Study of Two Dimensional Materials by Scanning Probe Microscopy

Ryan Plumadore

A thesis submitted in partial fulfillment

of the requirements for the degree of

Master of Science

in Physics

Department of Physics

Faculty of Science

University of Ottawa

Study of 2D materials by scanning probe microscopy

Ryan Plumadore

Abstract

This thesis explores structural and electronic properties of layered materials at the nanometre scale. Room temperature and low temperature ultrahigh vacuum scanning probe microscopy (scanning tunneling microscopy, scanning tunneling spectroscopy, atomic force microscopy) is used as the primary characterization method. The main findings in this thesis are: (a) observations of the atomic lattice and imaging local lattice defects of semiconducting ReS_2 by scanning tunneling microscopy, (b) measurement of the electronic band gap of ReS_2 by scanning tunneling spectroscopy, and (c) scanning tunneling microscopy study of 1T-TaS_2 lattice and chemically functionalizing its defects with magnetic molecules.

Acknowledgments

First and foremost, I would like to thank Professor Adina Luican-Mayer for her support and expert guidance throughout my master's degree. Words cannot describe how grateful I am for her mentorship over the past two years.

Thank you to Dr. Gregory Lopinski from the NRC, who allowed me to use (and often, to disassemble) their STM while we waited for our own to be installed.

Thank you to all the other students who worked within Prof. Luican-Mayer's group. In particular, thanks to Justin Boddison-Chouinard for many helpful discussions, whether with me or out loud to himself. Thank you to Vivian Chai for her work towards making devices for the STM, to Emmanuelle Launay for excellent AFM images, to Frank Amini and Colin Green for creating valuable figures and animations, as well as to Florence Grenapin and Ahmed Rezk for designing and testing the tip-making setup.

I would also like to thank Lukasz Andrzejewski for his suggestions and contributions to the tip-making setup, and Marco Taucer for his informative discussions on STM. Special thanks to Tony Olivieri for training me on almost every tool the CRPuO has to offer, as well as for his many useful tips on sample fabrication.

Finally, I am grateful to my friends and family who stood by me during this process.
To my father, for his unending support and encouragement.
To Juliana Kebic, for her love and patience throughout my studies.

August 2018

Contents

Abstract ii

Acknowledgments iii

List of Figures vii

List of Tables viii

1 Introduction **1**

1.1 Materials and Methods 2

2 Scanning Tunneling Microscopy (STM) **8**

2.1 Principle of STM 9

2.2 System Descriptions and Capabilities 14

2.2.1 Preparation of Samples for STM 22

2.2.2 Preparation of Tips for STM 24

2.2.3 STM Calibration 27

3 STM/STS of the Anisotropic Lattice and Defects in ReS_2 **31**

3.1 Results 32

3.2 Discussion 44

4 STM of the Atomic Lattice and CDW in 1T-TaS_2 **46**

4.1 Results 48

5 Conclusion and Future Work **52**

6 Appendices **55**

6.1 Additional STM Systems used for some data 55

6.2 Complementary Material 57

6.3 Tip Fabrication Through Electrochemical Etching 60

6.4 Tunneling Current Derivation 62

6.5 Manual Calculation of the Calibration Factors 64

List of Figures

1.1 Properties of TMDCs 3

1.2 Mechanical exfoliation procedure. 6

2.1 A one-dimensional rectangular barrier of height V_0 and width d. 9

2.2 Bardeen Formalism. 10

2.3 s-wave tunneling geometry. 12

2.4 RHK PanScan Freedom STM. 16

2.5 STM Head 17

2.6 Block diagram of STM feedback control system 18

2.7 STM Software User Interface 19

2.8 Double tip image. 20

2.9 Preparation of samples for STM. 22

2.10 Estimation of the lateral resolution in STM 24

2.11 STM tips imaged by scanning electron microscope. 25

2.12 Tip etching schematic and setup. 26

2.13 STM of graphite step edges 28

2.14 Graphite lattice schematic 29

2.15 Atomic resolution of graphite. 29

3.1 ReS_2 crystal 33

3.2 Large scale STM image of ReS_2. 34

3.3 ReS_2 showing diamond chain feature. 35

3.4 Atomic resolution image of ReS_2 surface, and associated 2D FFT 37

3.5 Average of 64 ReS_2 spectra taken on a 20×20nm grid. 39
3.6 Example of the method to determine the bandgap 40
3.7 Conductance map of ReS_2 41
3.8 Defects in ReS_2 band structure. 42
3.9 Representative images of defects in ReS_2 lattice. 43

4.1 TaS_2 Crystal 47
4.2 STM topography of TaS_2 CDW. 48
4.3 Images showing a variety of defects in TaS_2. 49
4.4 STM of TaS_2 with TBrPP-Co molecules. 50

6.1 NRC's Omicron STM-1 55
6.2 Resistance welding of tungsten tip in standard stm tip holder. 56
6.3 Argonne's homebuilt STM. 56
6.4 Scanning electron microscopes 57
6.5 Atomic force microscopes. 60
6.6 Full tip etching setup. 61

List of Tables

3.1 Lattice parameters of ReS_2 from literature 35

3.2 Band gap values of ReS_2 from literature 38

Chapter 1

Introduction

Materials with reduced dimensionality have a place of prominence in recent nanoscience research for their promise towards innovative technologies. The experimental realization of graphene opened new avenues of research into ultrathin materials, which encouraged studies of the physics of low dimensional systems. There is a growing interest in similar layered van der Waals crystals (i.e. two-dimensional (2D) materials), which includes the family of transition metal dichalcogenides (TMDC).

Scanning probe techniques are of particular use for 2D materials, where the entire sample is a surface. For example, scanning tunneling microscopy (STM) is used to probe the structure and electronic properties of surfaces at the nanoscale. This measurement technique involves an atomically sharp tip positioned close to a conducting surface to allow a quantum mechanical tunneling current to flow, which is used to image the surface structure and measure its local electronic states with atomic scale resolution. Optical or electronic transport techniques, which average over the bulk of the material, may not observe behaviour localized to the surface,[1] which is accessible to STM. Because information is measured only locally with the STM, it is also uniquely adapted to search for and study effects of impurities and defects.

One of the questions answered through this thesis relates to the nature of the anisotropic lattice structure of rhenium disulfide (ReS_2) within the 2D plane. In-plane anisotropy offers an additional functionality for developing novel devices, and is a relatively rare

feature among 2D materials. Thus, STM is used to image the atomic lattice of the crystal, one of the first direct experimental demonstrations of this structure. Measurements of the band gap of semiconducting ReS_2 through scanning tunneling spectroscopy (STS) are also presented.

A second theme explored through this thesis was the visualization of the atomic lattice and defects in the metallic compound 1T-TaS_2. Furthermore, a method was developed to chemically modify those defects using molecular species.

1.1 Materials and Methods

Graphite is a three-dimensional crystal of carbon atoms in a hexagonal lattice strongly bound by covalent forces in-plane. In the z-direction the crystal is held together only by weak van der Waals forces, which allows it to be separated easily using mechanical exfoliation — first demonstrated by isolating graphene from graphite in 2004.[2–4]

This simple technique allows the crystal to be stamped onto a substrate (typically Si/SiO_2 with 285nm oxide), often producing flakes of crystal only one atom thick. Graphene is therefore the thinnest material possible, at only 0.6nm. On appropriate surfaces, these flakes can be seen with a standard optical microscope, and their thickness can be estimated to within $\sim$3 layers of accuracy. Other techniques like atomic force microscopy (AFM) and Raman spectroscopy are used to confirm the thickness (layer number).

Graphene has demonstrated interesting properties, for example: high carrier mobility,[5] high thermal conductivity,[6] and significant optical absorptivity.[7] The difficulty of scalable, high quality sample preparation and the lack of a band gap in graphene have limited its applications in electronic devices, but despite this it continues to yield surprising physics – just recently it was shown that arranging bilayer graphene with an angle of 1.1° gives it intrinsic unconventional superconductivity.[8] The simplicity of graphene

makes it an ideal material for studying unconventional superconductivity, which otherwise has been difficult to understand.[9–11]

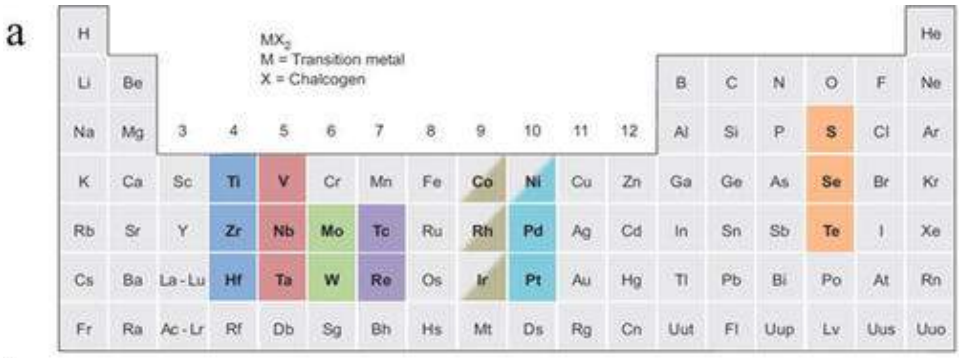

Bandgap (eV)		Mo	W	Ti	Zr	Hf	V	Nb	Ta	Ni	Pd	Pt
S	monolayer	1.8-2.1	1.8-2.1	~0.65	~1.2	~1.3	~1.1	metal	metal	~0.6	~1.2	~1.9
	Bulk	1.0-1.3	1.3-1.4	~0.3	~1.6	~1.6	metal	metal	metal	~0.3	~1.1	~1.8
Se	monolayer	1.4-1.7	1.5-1.7	~0.51	~0.7	~0.7	metal	metal	metal	~0.12	~1.1	~1.5
	Bulk	1.1-1.4	1.2-1.5	metal	~0.8	~0.6	metal	metal	metal	metal	~1.3	~1.4
Te	monolayer	1.1-1.3	~1.03	~0.1	~0.4	~0.3	metal	metal	metal	metal	~0.3	~0.8
	Bulk	1.0-1.2	metal	metal	metal	metal	metal	metal	metal	metal	~0.2	~0.8

Figure 1.1: TMDCs and their electronic structure.[12]

TMDCs have the general form MX_2, where M is a transition metal atom (groups 3 to 12 on the periodic table) and X is a chalcogen (sulfur, selenium, tellurium)(Figure 1.1a). Given the large number of possible constituent atoms, there exists a wide variety of TMDC combinations.[13–15] Much like in graphite, TMDCs are composed of weakly bound 2D layers.

Some TMDCs, like the metallic 1T-TaS_2, have been the subject of intense study over their unusual properties, such as charge density waves (CDW) and superconductivity.[16] Most semiconducting TMDCs have intrinsic band gaps in the visible range (Figure 1.1b) making them suitable for optoelectronic applications.[12] The reduction to monolayer thickness is accompanied by a transition from indirect to direct band gap.[17–19] The

ability to gradually reduce the dimensionality of these materials presents opportunities to study the quantum phenomena that occur at these extremes.

Monolayer materials are possible candidates for exploring spin-valley physics, and large spin-orbit interactions in these compounds lead to a splitting of the valence band due to the heavy transition metals, which in turn strongly affects their optical spectra.[20] Among the many properties 2D crystals show, semiconducting TMDCs (especially MoS_2 and WSe_2), have generated scientific interest for their strong spin-splitting and stable valley polarization enabled by the coupled spin and valley degrees of freedom.[21,22] Quantum dots made from them inherit this spin and valley dependence, showing promise for valleytronic devices.[23–25]

The combination of the intertwined spin-valley dynamics of excitons with the optical properties of TMDCs make them ideal systems for investigating excitons and their interactions with other electromagnetic excitations.[26] These materials have applications for studying excitons with intertwined spin-valley dynamics.[27–29] Their electronic and optical properties are promising for the development of high performance field effect transistors,[30,31] energy storage,[32] photodetectors[33–36] and solar cells,[35,37,38] and sensors based on changing resistance[39,40] or light emission.[41]

The research interest in 2D materials rests heavily on their out-of-plane anisotropy. Usually, their atomic lattice in-plane is symmetric. Breaking this symmetry opens the door to devices which have directional dependence, a feature not available to the other 2D materials.[42–45]

This thesis focuses on two TMDCs which exhibit periodic lattice distortions:

- **ReS_2**, which has an in-plane anisotropic lattice different from the hexagonal lattice seen in most TMDCs, and,
- **1T-TaS_2**, which exhibits a "Star of David" lattice deformation accompanied by charge density waves (CDW) at low temperatures (below 180K).

Isolating 2D Materials. A large focus of research in the field of 2D materials is the development and improvement of techniques to produce monolayers with controlled quality. The two principle methods for obtaining monolayers of crystals are top down (mechanical exfoliation) and bottom up (chemical vapour deposition).

Chemical vapour deposition (CVD) emerged as an alternative to mechanical exfoliation. Rather than isolating monolayer flakes from a large bulk crystal, in CVD, crystals are grown directly onto substrates. This gives precise control over the size and shape of samples, but is limited by its greater occurrence of sample defects.[46–49]

Exfoliation has the advantage of producing monolayer samples of high quality. Unfortunately, this technique is not scalable — producing a random pattern of flakes with varying thicknesses. They are limited to areas of about 30µm×30µm, and in practice only a few flakes on the substrate can be used at a time. The procedure for mechanical exfoliation follows.

First, silicon substrates with 285nm native oxide (obtained from Nova Electronic Materials), are cleaned by ultrasonication (8 minutes at 37 kHz) in acetone solution. Isopropanol (IPA) is used to rinse the acetone off the substrates, and then removed with a nitrogen gun. The substrates are then placed on a hot plate at 110°C to evaporate any remaining contaminants or vapour. Crystals are deposited onto silicon substrates (Si/SiO_2 with 285nm oxide) immediately using the mechanical exfoliation technique developed for graphene (Figure 1.2).

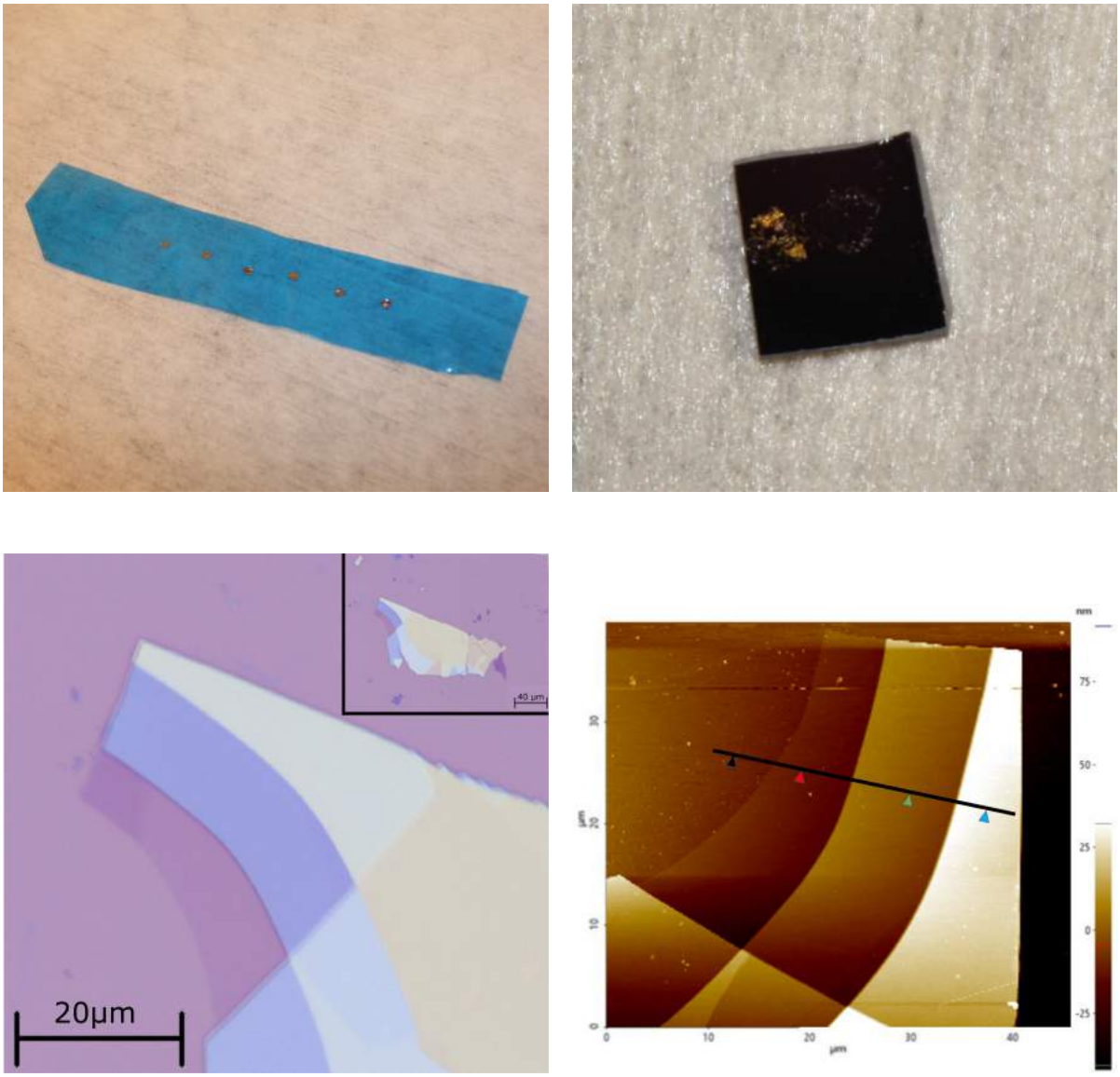

Figure 1.2: Mechanical exfoliation procedure. **(a)** Crystal is exfoliated several times on tape. **(b)** Crystal is pressed onto Si/SiO_2 substrate. **(c)** Optical image of graphene flakes (50X). **(d)** Atomic force microscopy image of (c), where the heights in the staircase structure can be measured relative to the substrate (black arrow): 2nm (red), 21nm (green), and 54nm (blue).

Thickness. Both mechanically exfoliated and CVD crystals can be located using an optical microscope. The thickness can be estimated to an accuracy within a few layers based on their colour and opacity - thinner flakes are more transparent, and appear as a

colour closer to that of the substrate. The thickest flakes are opaque and appear yellow to white. More rigorous characterization can be done using atomic force microscopy (AFM - described in Appendix 6.2) to measure the thickness of samples directly. An example of a sample characterized in this way can be seen in Figure 1.2d.

Chapter 2

Scanning Tunneling Microscopy (STM)

STM is a characterization technique used to probe the surface structure and electronic properties of materials at the nanoscale. Gerd Binnig and Heinrich Rohrer were awarded the 1986 Nobel Prize in Physics for this invention.[50] In STM, an atomically sharp tip and a metallic surface are brought close enough to allow a quantum mechanical tunneling current to flow between them when a voltage bias between these two is applied. Depending on the polarity of the sample bias, electrons flow from the tip to the sample (positive), or from the sample to the tip (negative).

In the most common operation mode, the tunneling current is kept constant with a feedback loop. By recording the change in tip height at each point (x, y) along the surface, this generates an array which represents a contour plot of the surface. If the tunneling current increases, the tip height is increased, and vice versa.

2.1 Principle of STM

In this section, the physical principle of STM will be covered. First, a simple one-dimensional system analogous to the tip-sample barrier will be used to explain the exponential order of tunneling current. The Bardeen Formalism in 2.1 describes tunneling phenomena in general, and Tersoff and Hamann applied this solution specifically to STM tunneling.

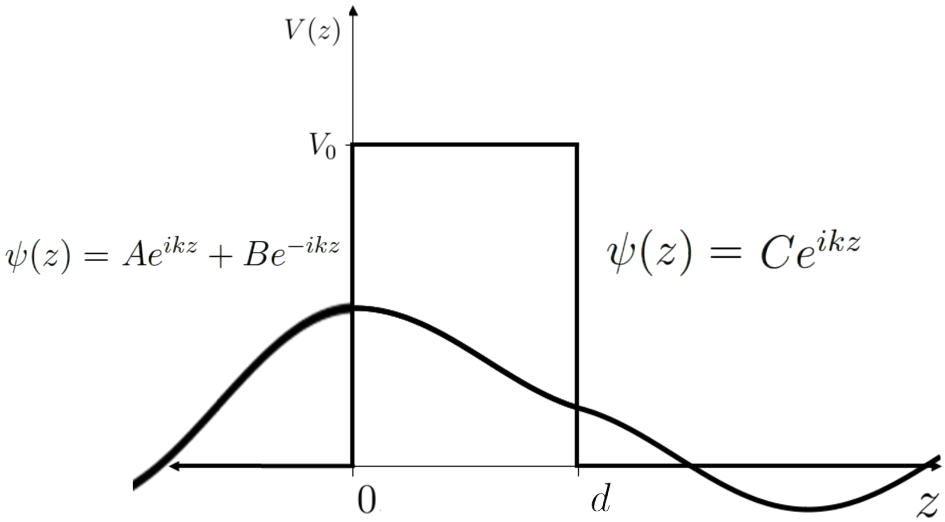

Figure 2.1: A one-dimensional rectangular barrier of height V_0 and width d.

Tunneling. Taking the simplified view of a one-dimensional barrier, like in Figure 2.1, assume we have a potential of height V_0 and width d. This potential acts as a barrier to the flow of electrons, which we can approximate as a barrier between two metal electrodes. For an incident wave with solutions $\psi(z)$, we will be able to solve for the transmission coefficient. By solving a system of equations described by the solutions inside and outside the potential (Appendix 6.4), we find[51] (with $K = \sqrt{\frac{2m}{\hbar^2}(V_0 - E)}$):

$$T = \frac{|C|^2}{|A|^2} \approx \frac{16E(V_0 - E)}{V_0^2} e^{-2Kd} \tag{2.1}$$

For electrons with energy E tunneling through a barrier potential of V_0, of width (tip-sample separation) d. The tunneling current is proportional to this transmission coefficient, which has an exponential decay in the barrier width:

$$I_t \propto e^{-2Kd} \tag{2.2}$$

and is thus extremely sensitive to the distance between the sample and tip, d. In practice, this feature is used to measure the topography of samples by maintaining a constant tunneling current during measurements. One does so by adjusting the barrier height while scanning, tracing a contour of the surface as the tip scans along. This is the most common mode used to obtain topographic information in STM.

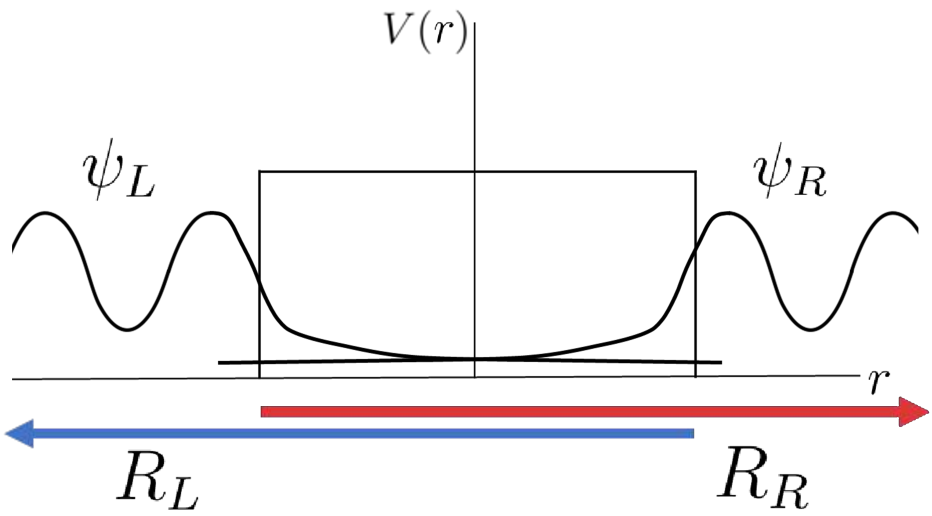

Figure 2.2: Separated system of Bardeen's Formalism.[52,53]

Bardeen Formalism. Tunneling can be more precisely described by using the Bardeen formalism, introduced in 1961 by John Bardeen.[52] This is a many particle approach which can be extended to describe tunneling phenomena, including STM tunneling. The basis of the formalism is to separate the system into two subsystems[53,54] with known Hamiltonians, H_L and H_R, for the left and right subsystems, R_L and R_R, as well as a "transfer" Hamiltonian, H_T, for the region in the middle.

The wavefunctions describing the left and right subsystems are $\psi_{L,i}(\vec{r})$ and $\psi_{R,i}(\vec{r})$. The rate of electron transfer can be found from the Fermi golden rule,[55] by considering the probability P of an electron to tunnel from the state $\psi_{L,0}$ to $\psi_{R,n}$:

$$P = \frac{2\pi}{\hbar} \sum_n \left| \langle \psi_{R,n} | H_R + H_T | \psi_{L,0} \rangle \right|^2 \delta(E_{R,n} - E_{L,0}) \tag{2.3}$$

Here the portion $\langle \psi_{R,n} | H_R + H_T | \psi_{L,0} \rangle$ is the tunneling matrix element, or M. The matrix element can be represented as:

$$M = \int_{-\infty}^{\infty} \psi_{R,n}^{\dagger} (H_R + H_T) \psi_{L,0} \quad d\vec{r} \tag{2.4}$$

Solving for M is difficult because the full Hamiltonian is not known. Bardeen's approach is to assume the Hamiltonian can be described by considering only H_L in R_L, and H_R in R_R. Since $\psi_i(\vec{r})$ decays across the barrier and is approximately zero in R_R, the assumption is that $H \cong H_R$ in that region. Similarly, $H \approx H_L$ in R_L. If we consider the integral in M over a surface separating R_L and R_R, it can be reformulated as:

$$M = \frac{\hbar^2}{2m} \int \psi_{L,0} \nabla \psi_{R,n}^{\dagger} - \psi_{R,n}^{\dagger} \nabla \psi_{L,0} \quad dS \tag{2.5}$$

The tunneling matrix element can now be calculated with only the wavefunctions $\psi_{L,0}(\vec{r})$ and $\psi_{R,n}(\vec{r})$. In applying this formalism to STM, we are hindered by the fact that the atomic structure of the tip, and therefore $\psi_{L,0}$, is not known in general. If we can solve for M through some simplifying assumptions, then we can calculate the transmission coefficient, equation 2.3.

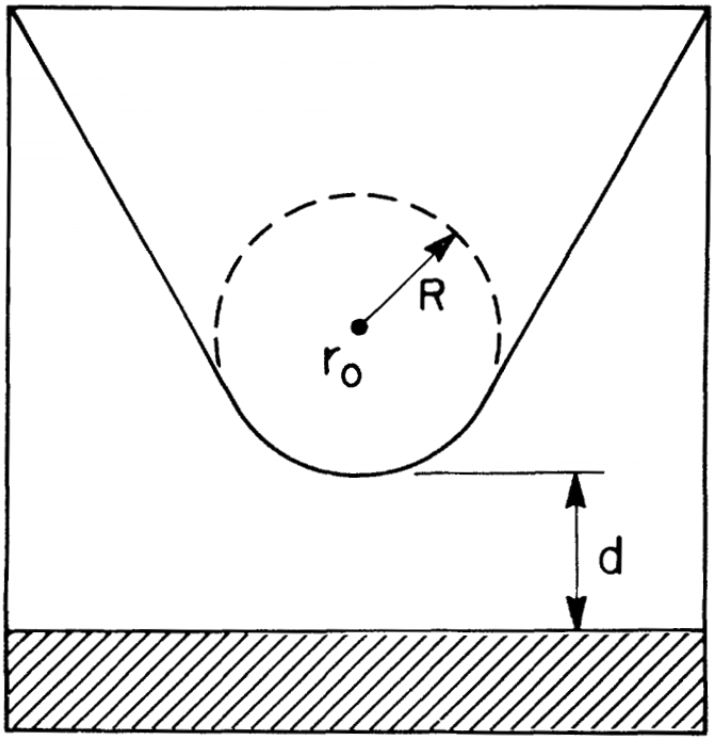

Figure 2.3: Schematic picture of tunneling geometry in the s-wave model. The shape of the tip is arbitrary, but is assumed to be locally spherical with radius of curvature R at its nearest point to the surface. Center of curvature is r_0, and the shaded region represents the sample.[56,57]

***s*-wave-tip model.** The first theory to apply the Bardeen formalism to STM was presented in 1985 by Tersoff and Hamann.[56,57] The tip is described by the simplest terms possible, as seen in Figure 2.3. In this theory, the sample will be weakly coupled to the tip, and tunneling will be mainly from tip states in the s-wave orbital (ignoring any angle dependent contributions). Perturbation theory is therefore suitable to solve for the junction. An expression can be obtained for the current which is independent of tip contributions.[58–60]

$$I = \frac{4\pi e}{\hbar} \int_{-\infty}^{\infty} \Big[f(E_F - eV + \epsilon) - f(E_F + \epsilon) \Big] \times \rho_{R,n}(E_F - eV + \epsilon) \rho_{L,0}(E_F + \epsilon) |M|^2 \quad d\epsilon \quad (2.6)$$

where $f(E)$ is the Fermi distribution function, E_F the Fermi level, V is the effective

local potential barrier height, and $\rho_{L,0}(E_F)$ is the density of states (DOS) of the tip at the Fermi level. The sample's DOS at the Fermi level is the remaining portion of the above expression:

$$\rho_{R,n}(E_F, r_0) = \sum_n \left|\Psi_n(r_0)\right|^2 \delta(E_{R,n} - E_F) \tag{2.7}$$

Since the wave functions decay exponentially in the z-direction, we get an expression relating this DOS to the distance to the sample, d, and the radius of the tip, R:

$$\Psi_n(r) \propto exp(-\chi z) \quad \Longrightarrow \quad \left|\Psi_n(r_0)\right|^2 \propto exp(-2\chi(d+R)) \tag{2.8}$$

The validity of this expression hinges on the assumption that the s-wave contributions from the tip are the most significant in STM tunneling. This has been shown to be true for most cases with free-electron model tips,[57,61–63] except in the case of tunneling to band-edge states.[64]

Spectroscopy. Equation 2.8 demonstrated again the exponential dependence of the tunneling current on the tip-sample separation. In equation 2.6, one can observe that the current is also proportional to the sample's DOS (equation 2.7).

In the limit of low temperature and small bias voltage, this expression for the current can be simplified, as $f(E)$ becomes a step function. In practice, this is the case as long as the energy resolution is greater than $k_B T$. By expressing M in terms of a current density operator and assuming it can be described by a step function as well, $|M|^2$ will be roughly constant within the region of interest.[52] In that case we can collect all the constants from the integral in equation 2.6 and get:

$$I \propto \int_0^{eV} \rho_{R,n}(E_F - eV + \epsilon)\rho_{L,0}(E_f + \epsilon) \quad d\epsilon \tag{2.9}$$

This expression tells us that the DOS of the tip and sample are equally significant in the

tunneling current. To measure the states in the sample, we need to eliminate $\rho_{L,0}$ from the integral. This is done experimentally by choosing tips made of metals which obey the free-electron model (typically transition metals, e.g. tungsten). In that case their DOS will be constant, and we get:

$$I \propto \int_0^{eV} \rho_{R,n}(E_F - eV + \epsilon) \quad d\epsilon \quad \Longrightarrow \quad \frac{dI}{dV} \propto \rho_{R,n}(E_F - eV) \tag{2.10}$$

This is applied in scanning tunneling spectroscopy (STS) by measuring the derivative of the current ($\frac{dI}{dV}$) while running through a range of bias voltage (V_b) values. Thus the local DOS of the sample can be measured through the derivative of the current (the 'conductance') with respect to the bias.

2.2 System Descriptions and Capabilities

Even small fluctuations in the tip-sample distance can have large impacts on the exponentially decaying tunneling current – environmental and electrical noise, thermal drift, sample and tip conditions and the tip-sample separation must all be controlled with sufficient accuracy to achieve atomic resolution.[54,59] Instrumentation designed to address each of these potential issues are described below. The primary STM used for these experiments was the RHK PanScan Freedom ("RHK STM"), so these descriptions will be focused on its particular components. Other systems used for a limited number of images in this thesis are described in Appendix 6.1.

Ultra-high Vacuum (UHV). Crucial to STM is the condition of the interface being measured. The sample must be isolated not only from external sources of noise, but also from sources of possible surface contamination. To that end, the STM is contained in a UHV system, meaning with pressures in the range of 10^{-9} to 10^{-11} Torr. Consider for example the time it takes a surface in air to be coated by the surrounding gas. Under

ambient conditions (760 Torr), the mean free path of molecules is about $70nm$.[65] At this pressure, a surface of $1cm^3$ will be covered in less than 1ns. At the typical pressure of experiments (10^{-10} Torr or less), this time is increased to 10^4s. To study clean interfaces, it is thus clear that UHV is the appropriate environment.

UHV imposes new design requirements for the STM unit compared to systems operated in air. The STM must be contained in a rigid, leak-tight environment (Figure 2.4). Outgassing becomes a serious issue, so the chamber is made of a low outgassing metal such as stainless steel. A periodic bakeout is required to remove adsorbed molecules from the chamber's inner surface out before achieving ultimate pressure.

In our set-up to achieve UHV three stages of pumping are used, each operating in a different range of pressures: roughing pumps bring the system to $\sim 10^{-4}$ Torr, then Titanium sublimation pumps (TSP) bring the chamber to 10^{-10} Torr, and finally ion pumps bring the system down to 10^{-11} Torr.

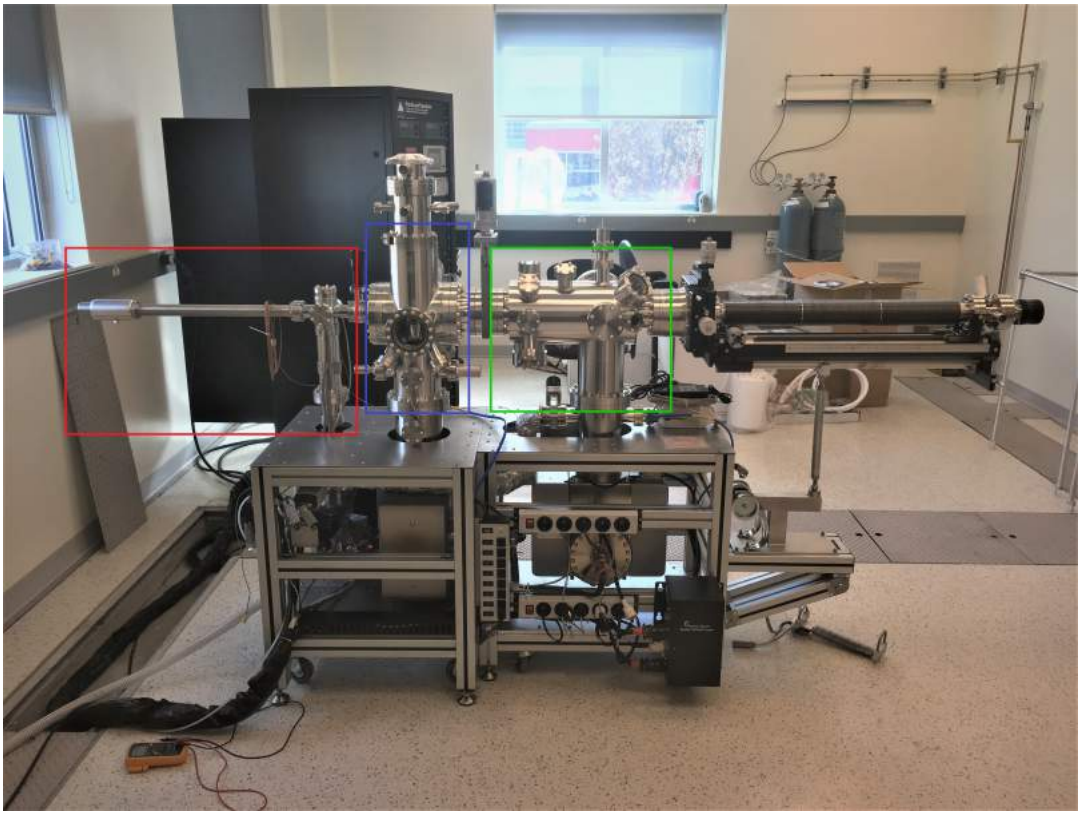

Figure 2.4: RHK PanScan Freedom STM. Red: Load-lock chamber and transfer arm. Blue: STM Chamber. Green: Sample preparation chamber.

To maintain this pressure, samples are introduced to the system through a "load-lock" chamber, which is isolated from the rest of the system with a gate valve. Pumping down the entire volume of the system from atmospheric pressure can take days – the much smaller volume of the load-lock is pumped down to 10^{-8} Torr in about an hour. The gate valve separating it from the STM chamber can then be opened to move samples in.

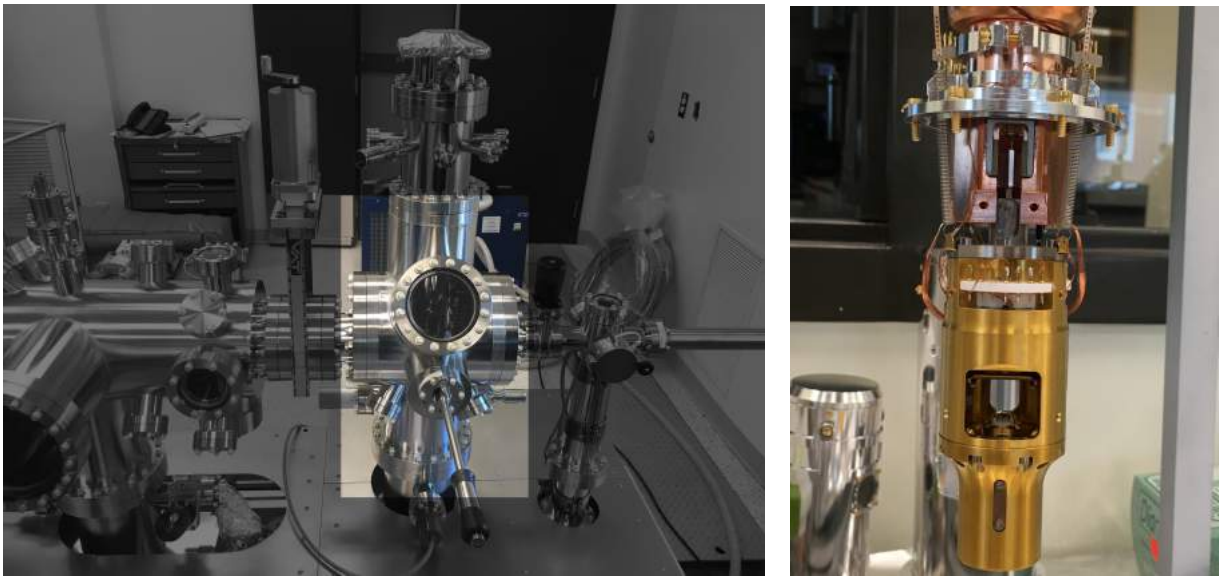

Figure 2.5: **(a)** STM chamber (highlighted area). **(b)** STM head, removed from the UHV chamber.

Low temperature is a feature which improves imaging in several ways. First, decreasing the temperature of the inner chamber can have a cryo-pump effect, adsorbing gases from the system onto the walls. Another issue eliminated by low temperature is thermal drift – dynamically varying fluctuations which limit the maximum achievable resolution. This is especially problematic for STS if one would like to measure spectroscopic data of a very specific point on the surface.

For the RHK STM used in this thesis, low temperature is maintained by a "closed-cycle" setup, which continuously recycles evaporated helium gas to bring the system to $9K$. Other low temperature systems might consist of a bath of cryogenic liquid in contact with the STM chamber, acting as a heat sink which cools the system.

Low temperature capability offers the opportunity to study physics which only occurs at extreme temperatures. An example in this thesis are the charge density wave modulations in 1T-TaS_2, which only occur below 180K.

Vibration isolation is also essential to STM. The exponential dependence of the

tunneling current on distance makes even small sources of noise significant. Noise from the building (5-10Hz), people walking across the floor (2Hz),[66] vehicles passing outside (5-25Hz),[67] and the STM's own pumps are all significant sources of noise. Several stages of passive vibration isolation are used to combat these: the pumps are isolated from the STM, and the system sits on a rigid table in a room which itself is separated from the building on a concrete slab. The STM head is mechanically rigid and is suspended by a spring suspension stage, part of which can be seen in Figure 2.5b. For the RHK STM, the closed-cycle cryostat is suspended above the STM chamber, and it must also be decoupled from the system to avoid transmitting vibrations during imaging.

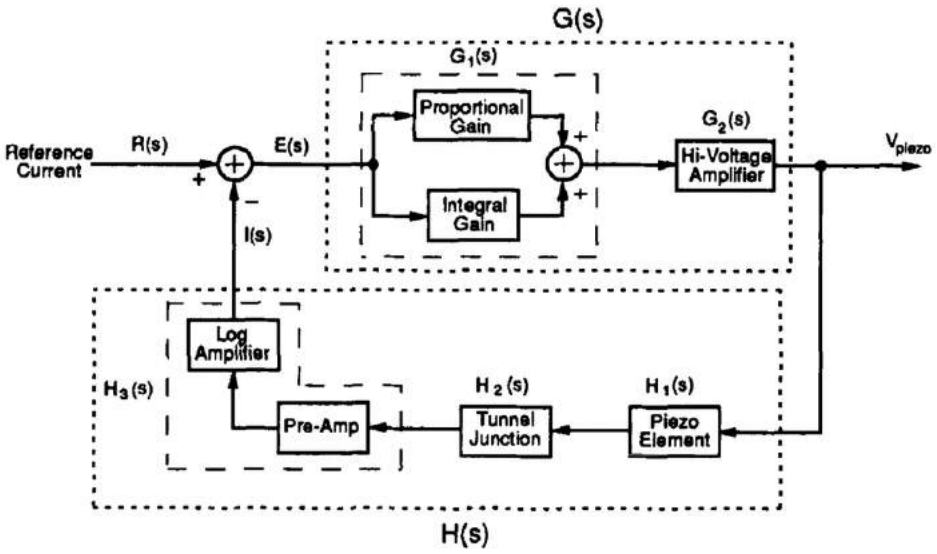

Figure 2.6: Block diagram for the feedback control system of an STM.[59]

Electronics for the STM must meet the required precision to control tiny fluctuations in current and voltage, while also minimizing electrical noise.

During scanning, the tip-sample separation will be on the order of $1nm$, and must be controlled with an accuracy of better than 1% of this value to produce meaningful results.[59] Pre-amplifiers help to overcome background electrical noise for the exceedingly small tunneling signal, which is on the order of pico- to nanoamperes. The exponential

signal then passes through a log amplifier to convert it to a linear signal. These have to be implemented with minimal capacitance and minimal distance from the tunneling junction to avoid electrostatic coupling and interference.

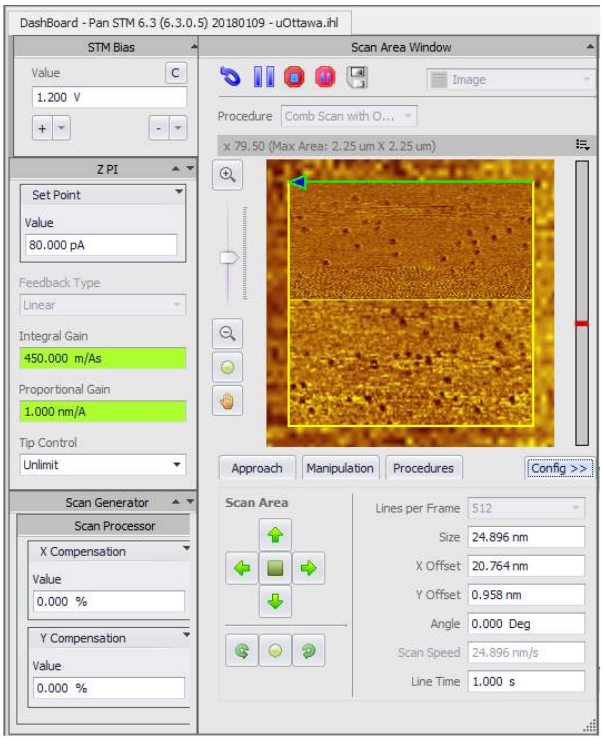

Figure 2.7: RHK STM User Interface. All of the parameters, including bias voltage, tunneling current, gain, scanning speed, and tip position are controlled through the software. The "Scan Area Window" shows data as it is being acquired.

A feedback loop[59] is used to control the tip-sample distance (Figure 2.6). For a fixed bias voltage and reference tunneling current chosen by the operator, the feedback loop reacts to the changing gap conditions to maintain a constant current, by adjusting the tip-sample distance. This is used initially to bring the tip into tunneling range, and during scanning the feedback loops reacts to the changing topography to adjust the height of the tip.

The feedback mechanism determines the ultimate scanning speed the system can reach – microsecond[68] response times can be achieved, but typical setups will have millisecond responses.[59] This is achieved through a combination of integral and proportional

gains, which can be adjusted between scans (Figure 2.7).

Tip positioning Coarse positioners are used to move the tip to different areas on the sample and to retract the tip. In practice, these move the sample plate relative to the tip, and sacrifice precision for larger range. During scanning, positioning is achieved through piezoelectric actuators ("piezos"). To image individual atoms, the tip must be able to move on this length scale accurately - piezos can achieve this resolution. The tip is controlled by a 4-quadrant piezo scan tube (fine positioners) which controls the X and Y motion, and another piezo which controls the Z motion. The range of the piezos is at most a few microns in either direction. While most of the electronics function within a range of $\pm 10V$, the operating range of piezos is on the order of $\pm 150V$. To fully extend the piezos, it is therefore necessary to include a high voltage amplifier (Figure 2.6).

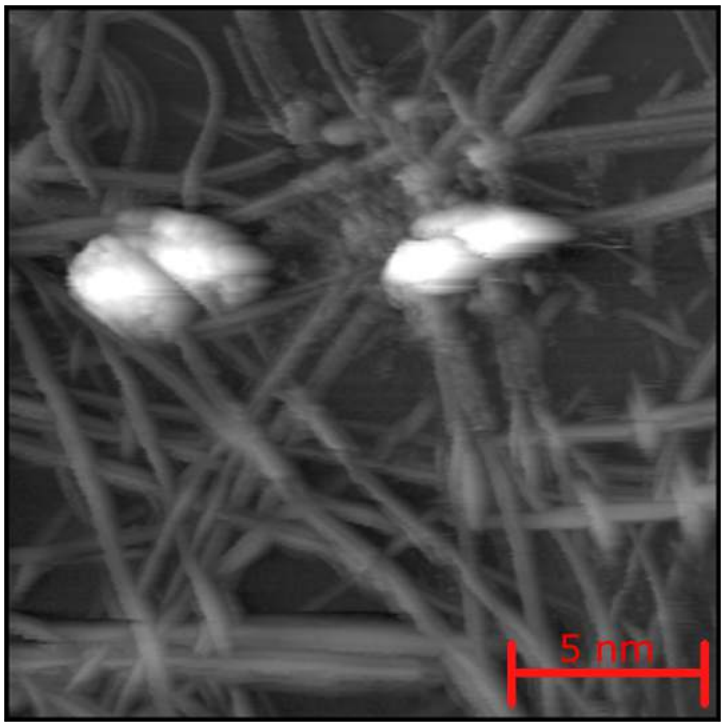

Figure 2.8: Image of carbon nanotubes from a double tip – each nanotube is visible twice in the image, as a result of tunneling through multiple tips.

Tip-sample preparation are crucial in STM. During scanning, the tip is typically

less than $1nm$ from the surface and can easily pick up adsorbed molecules and lose resolution. Tips must have a singular apex, else a "double-tip" effect occurs if there is simultaneous tunneling through multiple separate "tips" (Figure 2.8).

If the tunneling occurs through a non-metallic atom on the tip, the images will not represent the true electronic structure of the surface.[59] Consequently, with the goal of characterizing a surface, sample preparation is essential. But more than this, the surface should remain atomically clean for the duration of the experiment. The procedures for sample and tip preparation are described in sections 2.2.1 and 2.2.2, respectively.

2.2.1 Preparation of Samples for STM

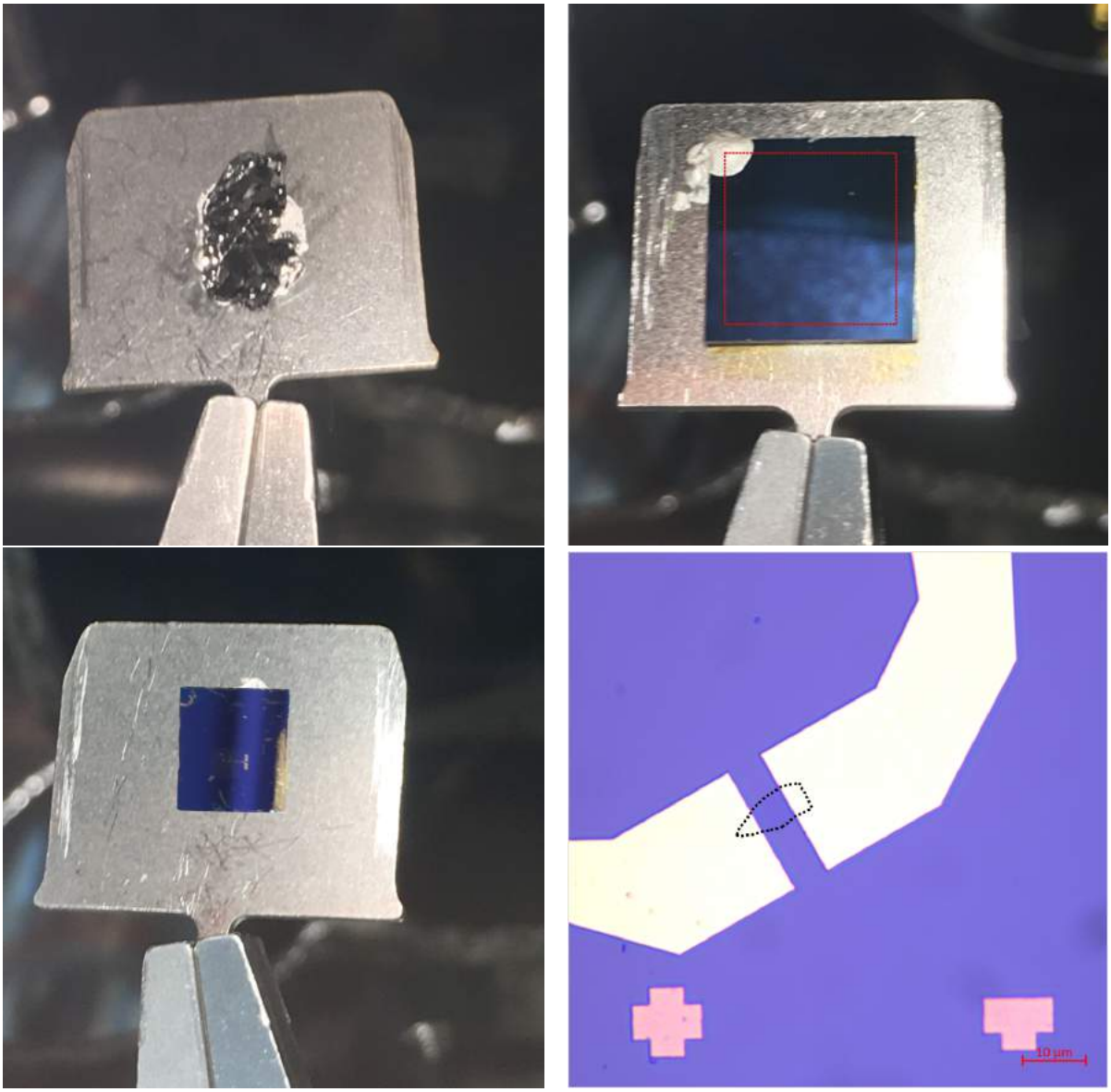

Figure 2.9: Preparation of samples for STM. **(a)** Natural graphite crystal on STM sample plate. **(b)** CVD graphene (red outline) on silicon wafer glued to sample plate. **(c)** Metal contacts connected to the sample plate. **(d)** Graphene (black outline) connected with gold contacts.

The experiments described later in this thesis are all on bulk crystals. The crystals are glued to STM sample plates with conductive silver epoxy (Epo-Tek H21D). Crystals

are quickly cleaved in air (less than 1 minute) before being introduced to the UHV environment to ensure the exposed surface is as clean as possible.

Substrates like Si/SiO_2 wafers are insulators. If the sample covers the entire substrate evenly (e.g. graphene grown with chemical vapour deposition) epoxy can be used to secure the substrate. Then, a small amount of epoxy can be applied on the corner of the sample down to the sample plate. The epoxy then electrically connects the sample to the plate.

In the case where samples are prepared through mechanical exfoliation, the area of a crystal flake is on the order of $10\mu m$. To achieve this size and to make contact to the STM plate, the following procedure is used. Seeing that the samples examined in this thesis were all bulk crystals, only an outline for the preparation of exfoliated samples will be given here.

Beginning with a clean silicon substrate (Si/SiO_2 with 285nm native oxide), we use standard e-beam lithography to connect the chosen flake to sample plates. First, a grid of small features is created on the surface. The regular sample fabrication methods are used to get the desired sample onto the substrate (Figure 2.9d). Using the grid for alignment, contacts can be very precisely placed just on the edges of the sample, leading off to larger metal pads far from the sample. Using a wire bonder these larger pads allow the sample to be integrated in devices, or simply connected to an STM sample plate (Figure 2.9d). In this way, conductive samples can be prepared for STM, regardless of their size or the substrate's properties.

2.2.2 Preparation of Tips for STM

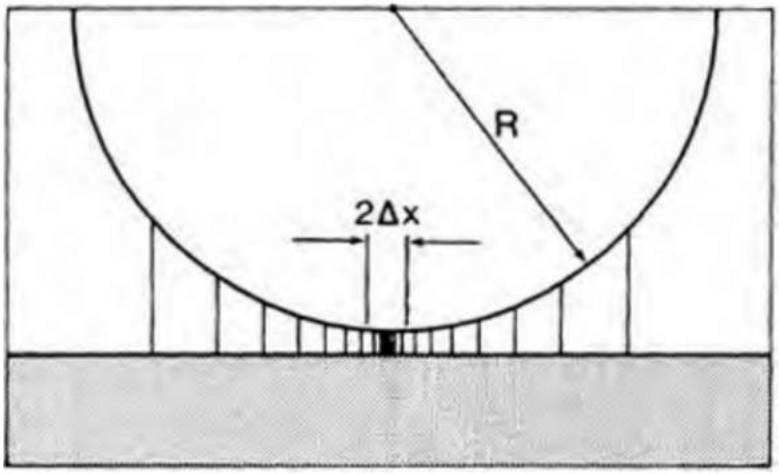

Figure 2.10: Estimation of the lateral resolution in STM. The tip apex, with radius R, is very close to the sample surface. The tunneling current is concentrated in a small region around the origin, $x = 0$. With $R = 100$ nm, the radius of the tunneling current column is approximately $\Delta x = 4.5$ nm.[54]

In order to obtain high resolution images in STM, it is crucial for the radius of the tip at the apex to be as narrow as possible (Figure 2.10). In order to resolve individual atoms, it is therefore essential to achieve the smallest value for R possible. Tips with radius below 100nm can be achieved regularly and will give good resolution, but the sharpest tips have radius below 20nm (Figure 2.11b). Two principal methods exist for the fabrication of tips: the pull-and-cut technique and the chemical etching technique.

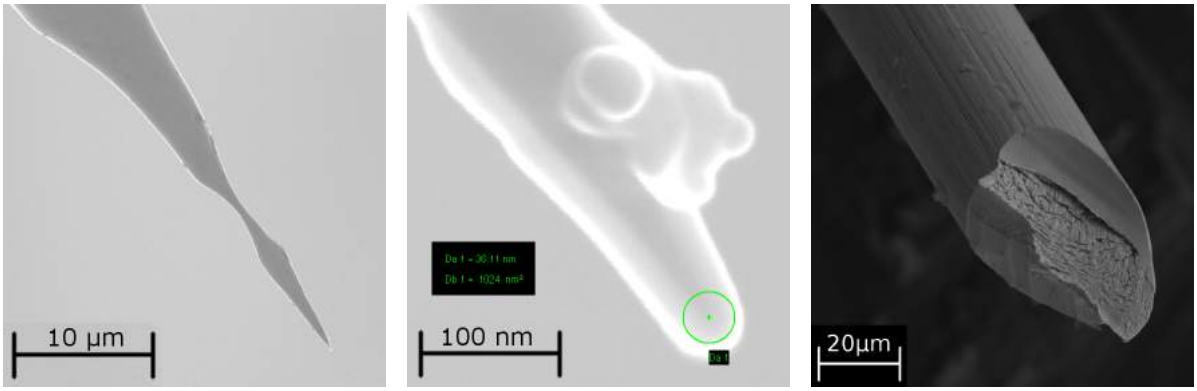

Figure 2.11: STM tips imaged by scanning electron microscope. Working distance: $5.7mm$. **(a)** Etched W tip. **(b)** Higher magnification view of (a), with measured radius of curvature $18nm$. **(c)** Mechanically cut qPlus AFM/STM W tip.

The pull-and-cut technique is primarily used for Pt/Ir tips. Here, wire cutters are used to grip the end of the wire. The other end is held with tweezers and the wire cutters are pulled away while cutting. SEM images of such tips reveal a rough structure macroscopically, but with only a small radius at the apex nonetheless (Figure 2.11c). Since the tunneling current is exponential, only these atoms at the tip apex contribute. Therefore this method is suitable, so long as the apex ends up with the correct shape.

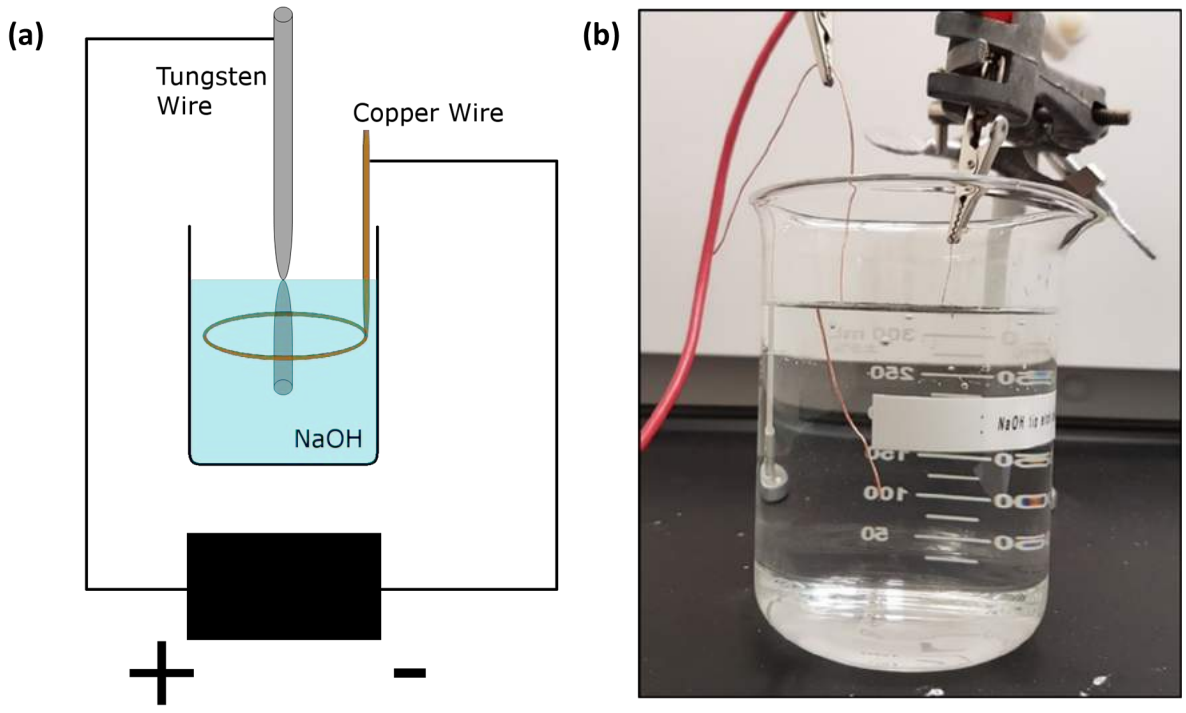

Figure 2.12: Tip etching setup. **(a)** Schematic. The black box represents the power supply which controls the current and voltage during etching. **(b)** Experimental setup.

For tungsten (W) tips, an etching setup was constructed (Figure 2.12). This setup is designed to prepare tungsten tips through a one-step electrochemical etching process. Tungsten wire (0.25 mm diameter) is submerged in 2M NaOH solution, and a ring of copper wire completes the circuit. A current is applied between the two wires, gradually thinning out the tip at the meniscus of the solution, where the W can react with both the NaOH solution and O_2 from the air. When the wire is so thin that it cannot support the weight of the submerged wire, it will break, resulting in a sudden voltage drop as the circuit is broken. The tip is then retracted and cleaned before being used for STM. The details of this procedure can be found in Appendix 6.3.

Tips with sharpness as low as 18nm have been obtained using this method, as seen in the SEM images in Figure 2.11.

Commercial W tips have been used in addition to tips fabricated in the lab. Comparison with SEM has shown the tip radius to be similar to those produced by the method described here.

2.2.3 STM Calibration

In this section, STM results on natural graphite (Graphit.de) samples, prepared using the method described in 2.2.1, are presented. These images are used to calibrate the piezos which control the tip motion during scanning. For the STM images to be scaled properly, each piezo must move by the same amount for the same applied voltage. These piezos will expand when an electric field is applied, and the relationship between the expansion and the applied voltage is constant. By determining this constant factor, each piezo can be adjusted to have the same proportionality between applied voltage and expansion.

In order to set the correct constant factor for each piezo, one has to measure a known structure with atomic resolution. The well-known values for the lattice parameters of graphite, its distinct band structure and simple elemental composition make it a typical candidate for calibration. The following section describes calibration of the STM with graphite samples.

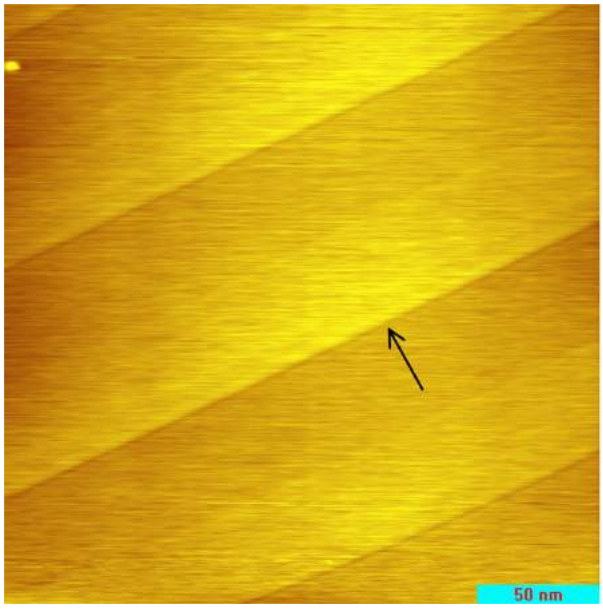

Figure 2.13: STM of graphite step edges. V_b=0.1V ; I_t=500pA. Size=250nm. Taken with RHK STM.

Topography. The procedure for imaging bulk 2D crystals begins with imaging larger areas (on the order of a few hundred nanometres). In doing so, we can find step edges on the surface, as seen in Figure 2.13. Finding these steps is the initial stage in attempting to resolve the surface, as it helps to confirm the sample is relatively free of contamination. Once the step edges are located, the lattice is imaged by moving onto the terraces and reducing the scan size gradually. Graphite is better resolved with a low bias voltage (V_b=100mV) and a high tunneling current (I_t=500 pA).

Consider for example Figure 2.14, which shows a schematic of the atomic lattice of graphite. The atomic layers of graphite consist of a hexagonal lattice in $A - B - A$ stacking, meaning the atoms of the second layer are offset from the first by one unit cell distance. Half the atoms in a hexagon will be aligned above a carbon atom in the next layer (α atoms), and half will be above an empty space (β atoms).

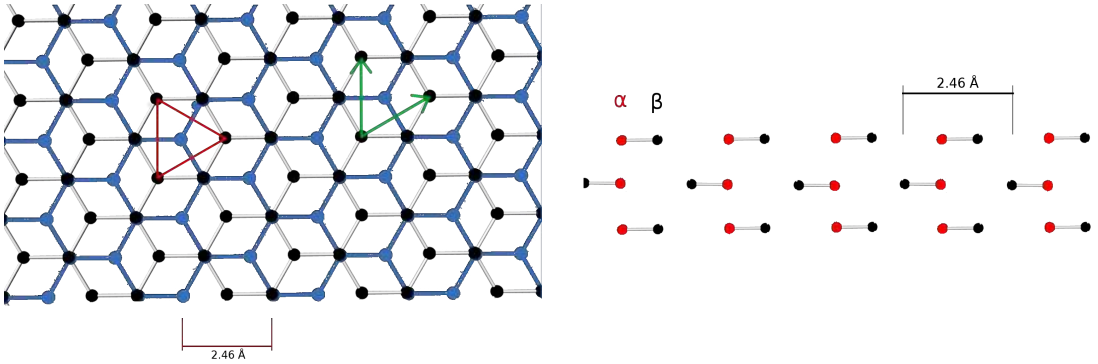

Figure 2.14: Graphite lattice schematic in $A - B - A$ stacking. **(a)** Top-down view of two layers. Red triangle represents the observed topography in STM. **(b)** Side-view. The length of one period ($2.46\mathring{A}$) used in the calibration measurements is indicated, and the A and B vectors are drawn as green arrows.

Due to the stacking between layers, two dissimilar sets of three carbon atoms exist. This inequivalence is reflected in the electronic structure, as observed by the STM (Figure 2.15), where only half the atoms in the surface layer are observed. Instead of a hexagonal lattice, a triangular lattice showing every other atom is seen (for a total of 3 per hexagon).[69–73] It was suggested that the β atoms have a greater contribution to the tunneling current at low bias, but it is possible to switch between α and β sites by alternating the bias polarity.[69] In graphene, where such stacking is not present, the hexagonal lattice is observed once more.[74]

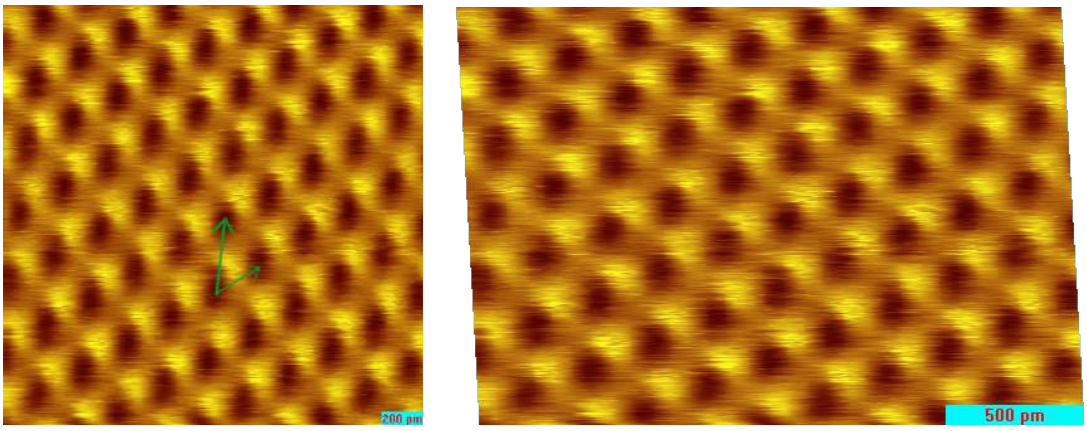

Figure 2.15: Atomic resolution of graphite. V_b=0.1V ; I_t=500pA. Size=2nm. Taken with RHK STM. **(a)** Raw image before calibration, green arrows indicate the A and B vectors. **(b)** Final recalibrated image.

Calibration of the STM is done by first obtaining the atomic lattice of graphite, as in Figure 2.15a. The lattice is well resolved and the expected triangular contrast is suitable for calibration. Since the lattice constants of graphite should both be equal ($a = b = 0.142$ nm), we can compare the values we get for each with the expected values to determine all the necessary scaling parameters. These parameters describe a stretch in the x- and y-axis to correct the magnitudes of the vectors, as well as a skew factor to correct the angle between them. These constants describe the correction on the piezos.

Calibration on the RHK system will be explained based on Figure 2.15a. The "A" and "B" vectors are drawn manually on the image (green arrows in Figure 2.14a and 2.15a), and the number of periods along these vectors is counted. For these measurements, a period is defined to be across the center of adjacent hexagons (0.246 nm), so that measurements are made from the dark spots in the images.

By inputting the correct values for the lattice parameters, the program calculates the factors for x, y, and the skew. For this particular image, these are $x = 1.098$, $y = 0.758$, $skew = -3.2°$ — the result is Figure 2.15b. While the borders of the image are no longer square due to the skew applied, the hexagonal lattice is now perfectly symmetric. Scans taken after this recalibration will be prescaled by the STM to have square image frames.

Chapter 3

STM/STS of the Anisotropic Lattice and Defects in ReS_2

ReS_2 is a layered material consisting of Rhenium (Re) metal atoms (group VII) with Sulfur (S) chalcogens. Compared to crystals like MoS_2, which arrange in a hexagonal lattice, this TMDCs has one extra valence electron. The result is a Peierls distortion, where Re atoms move together, favouring metal bonds in diamond-shaped clusters of intralayer chains[75,76] (Figure 3.1a). The crystal structure is a distorted 1T-triclinic in the $P\overline{1}$ space group, featuring in-plane anisotropy[77] typical of d^3 TMDCs. It is a semiconductor with a band gap of approximately 1.5 eV. There is much debate as to whether this gap is direct or indirect, and to what degree the interlayer coupling contributes.[45,78–87]

Transistors fabricated from the material show an on-off ratio of 10^6 or greater[82,88] making it an excellent candidate for transistor applications. It is useful as a catalyst and is considered stable in air.[89,90] ReS_2-based devices have potential as components in solar cells, as polarization-sensitive detectors, or in optical computation and logic circuits in the infrared region.[91,92]

The anisotropic chains are thought to weaken the interlayer coupling, causing stacked layers to decouple.[85] The result would be a bulk material in which the bulk band gap remains direct.[85] In addition, the layers are not symmetric vertically; an upside-down layer has the orientation of properties reversed.[93] Evidence of the anisotropy

is seen in its polarization dependent band gap.[94] Electrical transport measurements have shown anisotropic resistivity which allows identification of lattice orientations.[95] Scanning transmission electron microscopy (STEM) and transport measurements have shown a direct correlation between its anisotropic electron transport and the orientation of the anisotropic lattice chains.[85]

Previously, the lattice of ReS_2 has been visualized primarily by transmission electron microscopy (TEM)[85,96] and X-Ray spectroscopy.[83,97] Only a few STM attempts, which were not able to fully visualize the lattice, have been attempted.[98–100] The electronic structure has also been studied with several theoretical calculations[45,79,84,85,90,101] and experimental methods, including optical[78,79,81–83,85,87,102,103] and electronic transport[80,86,87] measurements.

3.1 Results

The goal of these experiments was to measure with STM the atomic lattice of ReS_2, including the anisotropic distortion, and to measure the band gap of the crystal through STS. Commercial (HQ Graphene) ReS_2 crystals were prepared as described in Section 2.2.1 and exfoliated before being introduced to the STM. We noticed that below ∼80K, we were unable to reach tunneling conditions. For that reason, experiments were performed either at 80K or room temperature.

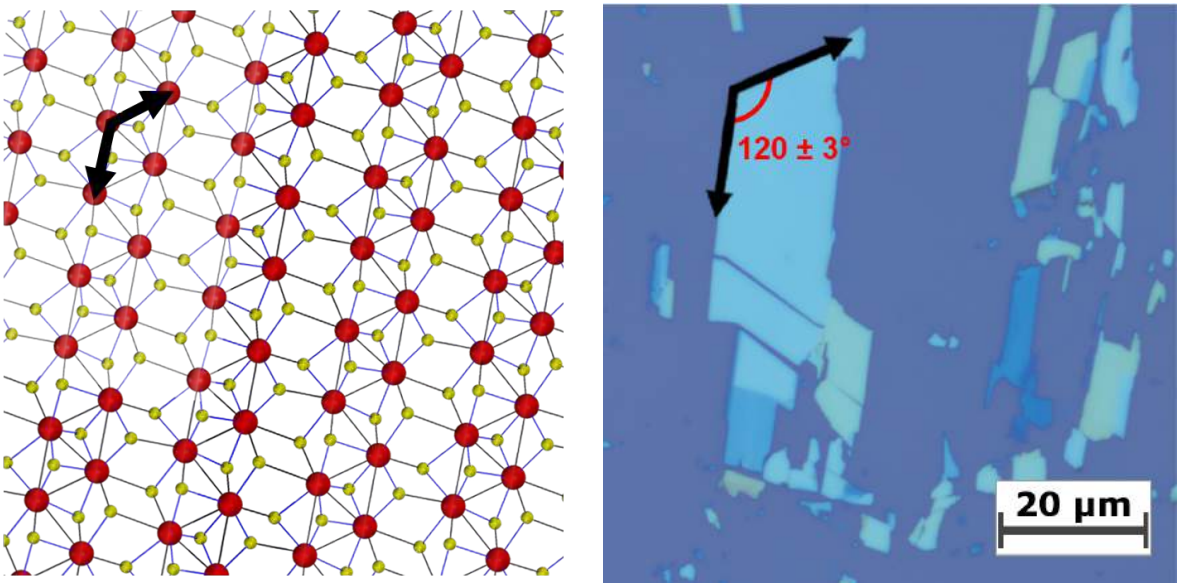

Figure 3.1: ReS_2 crystal. Lattice directions are indicated with black arrows on the schematic and exfoliated flake. **(a)** Lattice structure (top-down view). **(b)** Exfoliated ReS_2 on silicon wafer.

The lattice of ReS_2 (Figure 3.1a) was resolved by first locating step edges in the material. It is interesting to see that much like with exfoliated flakes (see Figure 3.1b), the anisotropy of ReS_2 is evident in the topography (Figure 3.2). Furthermore, an angle of $120\pm3°$ consistently appears at the corners of such flakes/terraces. This angle is the same as the one between the in-plane lattice parameters for ReS_2. These observations indicate that the crystals preferientially break along the chain direction, which gives us a macroscopic way to identify the lattice orientation of ReS_2 samples. For example in Figures 3.1b and 3.2 one can assume that the lattice chains are oriented in the same way as the long, narrow flakes/terraces in the optical/STM topography images.

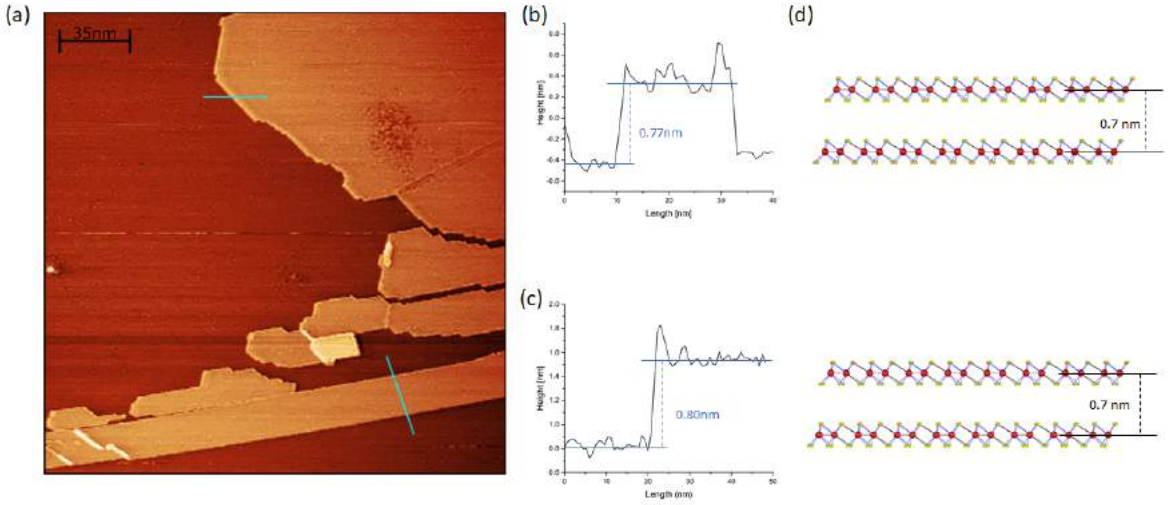

Figure 3.2: Large scale STM image of ReS_2. **(a)** STM Topography of ReS_2. V_b=-1.6V ; I_t=450pA. Size=220nm. T=300K. Taken with Omicron STM-1 at the NRC. Height profiles across the blue line at the **(b)** top and **(c)** bottom right of the image show terraces of about $0.8nm$. **(d)** Side-view of two layers of ReS_2 crystal, aligned with the profiles.

The ideal scanning parameters for atomic resolution on ReS_2 are less well-known than those for graphite, as there have only been a few reported attempts at imaging this crystal with STM.[98–100] Both high voltage (above 1.0V in magnitude) and current (above 350pA) were found to be ideal for imaging the atomic lattice.

Lattice Parameters ($\AA$)	Technique	Ref.
$a = 6.352$, $b = 6.446$, $\gamma = 120°$	NanoARPES at 100K	80
$a = 6.51$, $b = 6.41$	DFT - ATK	84
$a = 6.41$, $b = 6.48$ $\gamma = 119.03°$	HREELS, TEM	86
$a = 6.352$, $b = 6.446$	ARPES	80
$a = 6.417$, $b = 6.510$, $\gamma = 121.10°$	X-Ray	97
$a = b = 6.4$	STM	99
$a = b = 6.5$	STM	100

Table 3.1: Table of lattice parameter values of ReS_2 from literature.

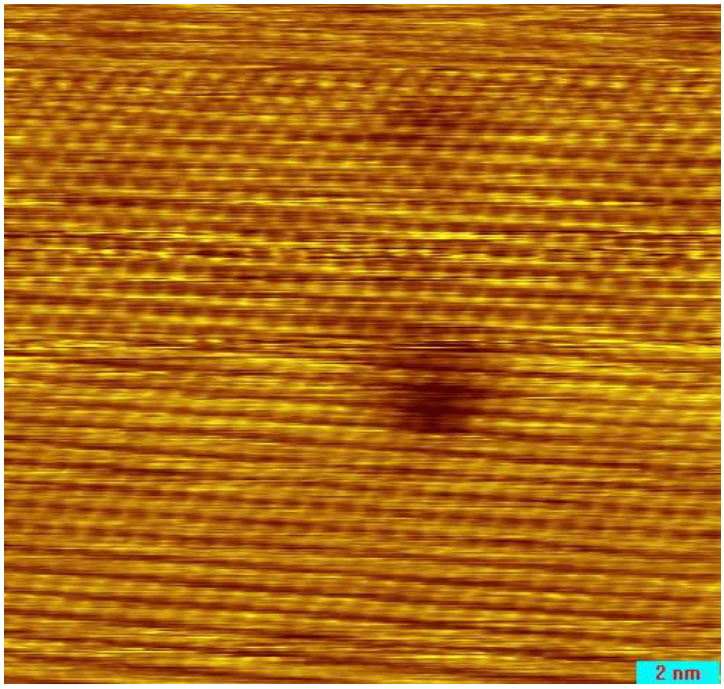

Figure 3.3: ReS_2 showing diamond chain feature for part of the scan. V_b=1.20V ; I_t=80pA. Size=4.34nm. Taken with RHK STM.

Figure 3.3 is a representative image where only the diamond clusters are resolved, and not the individuals atoms – to confirm these are the diamond clusters, measurements were done on 15 such images. The values for the lattice parameters which define the distances between unit cells, a $(0.59 \pm 0.05nm)$, b $(0.62 \pm 0.06nm)$, and γ $(119 \pm 6°)$, agree well with those from the literature (Table 3.1).

Atomic resolution is shown in Figure 3.4a, taken at a bias of 1.20V and current of 400pA. To determine whether we are observing 4 Rhenium atoms in diamond clusters,

or the Sulfur atoms, additional measurements were done on images like Figure 3.4 to determine the distance between the atoms within a given unit cell. Unlike in many TMDCs where the two types of atoms have the same hexagonal symmetry, in ReS_2 the surface atoms have different symmetries. Based on the references in Table 3.1, the Re atoms within a unit cell are arranged in a symmetric parallelogram, with all sides measuring ≈0.30 nm. A hexagonal symmetry exists for the S atoms if one considers only the top or bottom layer of S atoms. Since the Re_4 chains are 0.20nm wide but are separated by gaps of 0.34 nm,[89] it is not possible to overlay this hexagonal symmetry onto the Re atoms – this would instead result in a distorted hexagon. From careful measurements, it is therefore possible to verify the type of surface atom imaged in ReS_2 from the structure observed in the STM topography alone.

In prior STM studies of ReS_2, reports have been conflicting as to which surface atoms are observed. Though most have indicated that they observed the sulfur atoms,[99,104] some have claimed to see the rhenium atoms.[100] Though we have not yet determined why this discrepancy exists, it is likely due to differences in scanning parameters. The studies which observed sulfur atoms all indicated high tunneling currents and positive bias voltages, while ours and the others reporting rhenium atoms had negative bias voltage or lower tunneling currents. Our measurements indicate distances of 0.35 ± 0.04 nm between nearest atoms in a unit cell. From the fact that this distance is symmetric within diamond shaped clusters, and that no atomic hexagonal symmetry is observed, it is possible to conclude that the images are of Re metal atoms.

These measurements are also supported by the 2D Fast Fourier Transform (FFT) of the topography image. The innermost points (orange) represent the anisotropic lattice chains – the brightest four correspond to the striped pattern across the lattice, and the rest are associated with the hexagonal structure of 7 unit cells. The surrounding points (blue) correspond to the atoms seen in the image. Measuring the inverse distances

between these points can be used to determine their separation in the real space image, and from these values the same conclusion can be reached that Re atoms are observed in the topography.

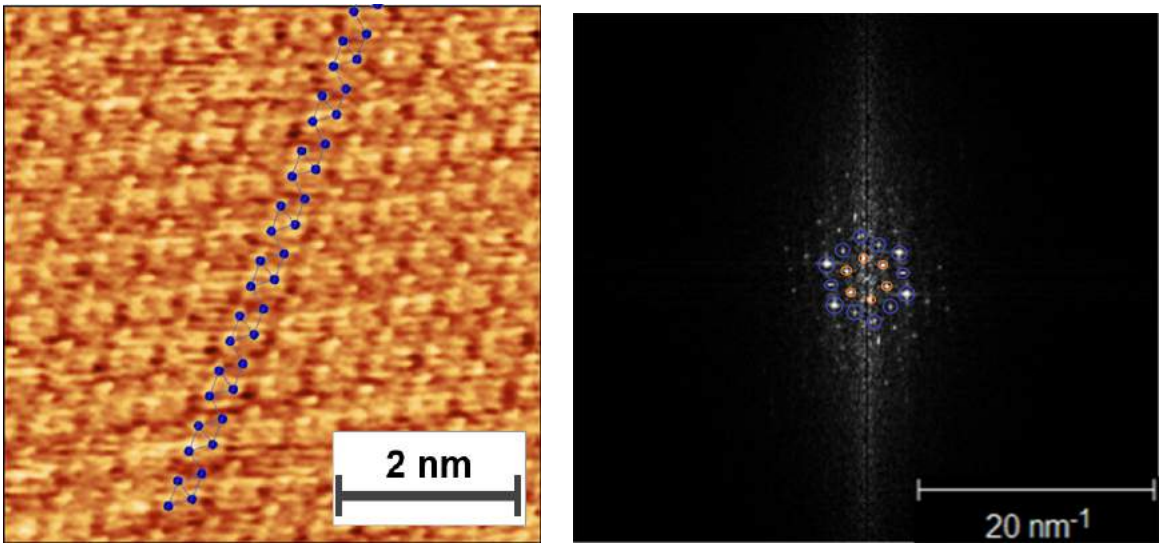

Figure 3.4: **(a)** Atomic resolution image of ReS_2 surface, with Re-atoms along a chain are highlighted in blue. V_b=-1.95V ; I_t=400pA. Size=5nm. Taken with Omicron STM-1. **(b)** 2D FFT of (a). Points with the brightest intensity are highlighted.

Spectroscopy. A collection of band gap values from many different experimental and theoretical techniques is presented in Table 3.2. While they are in conflict as to the nature of the semiconducting gap, these sources have all reported values which fall within a consistent range: $1.5 \pm 0.1eV$. The value we measured with STS agrees with this at $1.3 \pm 0.3eV$, but is set apart as the first reported value of the band gap from scanning tunneling spectroscopy. This measurement differs from the optical and electron techniques by measuring the gap locally, as opposed to taking an average over the entirety of the crystal.

Bandgap (eV)	Technique	Type of Sample	Ref.
1.41±0.05	IL-gated FET	15-25nm mechanically exfoliated on SiO_2	78
1.57, *1.85*	K-space photoemission ion microscopy, [DFT]	Mechanical exfoliation transfered onto HOPG	79
1.49*, **1.53****	NanoARPES at 100K at $\Gamma^{\star}$ or $Z^{\star\star}$ point	Commercially grown, cleaved in UHV	80
1.47, *1.65*	Photoluminescence (PL)	CVD	81
1.50, 1.54†	PL	CVD, †tri-layer	82
1.55±0.04	PL	Dispersion preparation from powder	102
1.51	PL	Mechanically exfoliated on SiO_2	83
1.47, *1.61*	PL	Mechanically exfoliated on PDMS	103
[*1.43*]	DFT - GGA	*n/a*	101
[**1.50**]	DFT - ATK	*n/a*	84
[*1.36*]	DFT	*n/a*	45
[*1.42*]	DFT	*n/a*	90
1.42, *1.52*	HREELS, TEM	Drop-casted powder	86
[**1.35**, *1.43*], **1.55**	PL, DFT	CVD	85
1.36$^{\perp}$, **1.51**$^{\parallel}$	Optical and SEM	CVD	87

Table 3.2: Table of bandgap values of ReS_2 from literature. Bulk values are presented in bold, monolayer values in italics and theoretical values in square brackets. Average of band gaps $= 1.5 \pm 0.1eV$.

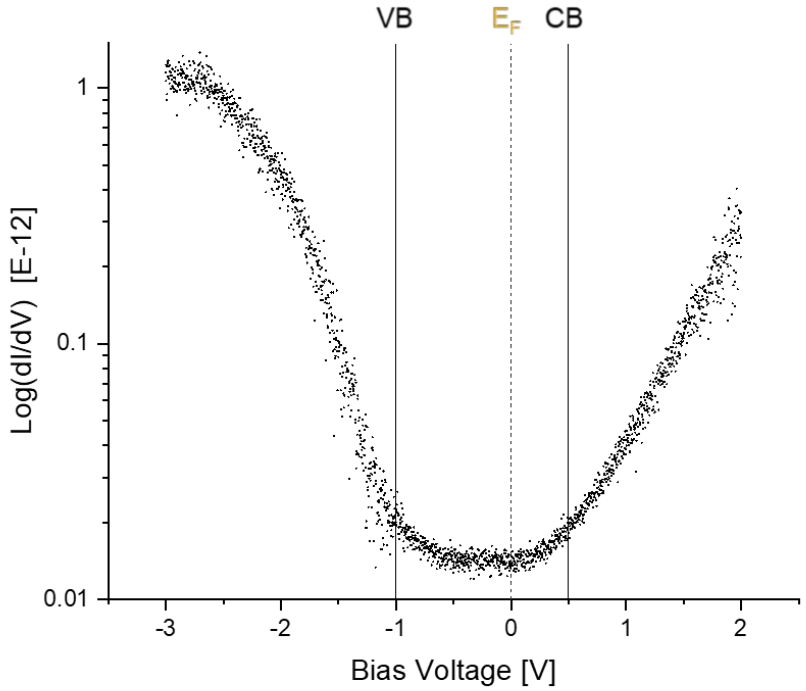

Figure 3.5: Average of 64 ReS_2 spectra taken on a 20×20nm grid.

Figure 3.5 represents a typical spectrum on ReS_2, with the positions of the valence band (**VB**), Fermi level (E_F) and conduction band (**CB**) demarked. In general, we see that the Fermi level is closer to the conduction edge on the right. This indicates that the crystal is n-doped, which agrees with other studies on ReS_2.[78,95,101]

Since both Cl and Br are used as halogen transport agents in the synthesis of ReS_2, it is likely that they substitute for some Re atoms in the lattice. This would explain the n-doped character seen in the spectroscopy, as Cl/Br doping is known to induce n-doping in this crystal.[105]

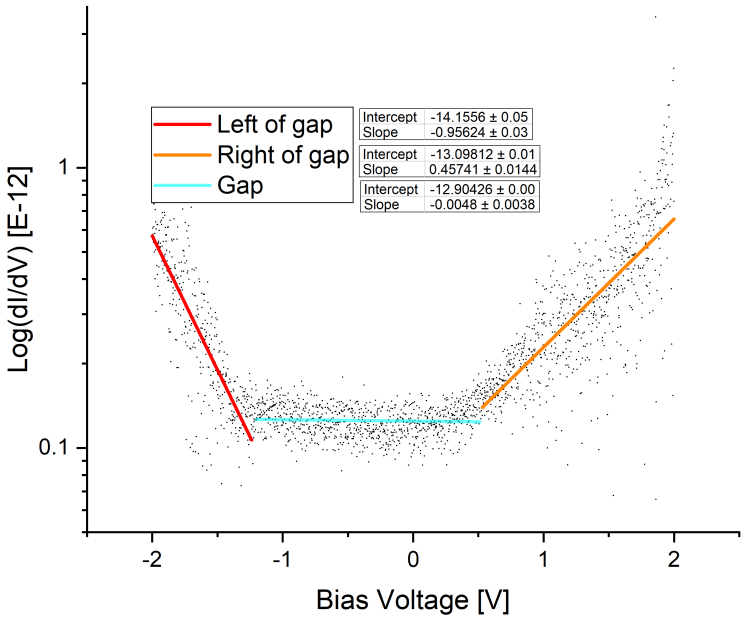

Figure 3.6: Example of the method to determine the bandgap. Average of 20 spectra taken at a point.

From our spectra, we are able to determine the bandgap of ReS_2. To measure the gap, we first take a log plot of the dI/dV graph from the measurement. A linear fit is taken on the portions just to the left (valence band) of the gap and to the right of the gap (conduction band). Calculating the intersection of these lines with a third linear fit within the gap determines the left and right edges of the gap interval. The length of this interval in x is taken to be the value of the band gap, with uncertainties determined from the linear fits. An example is presented in Figure 3.6. By averaging 790 total spectra, this method gives our value of $1.3 \pm 0.3eV$.

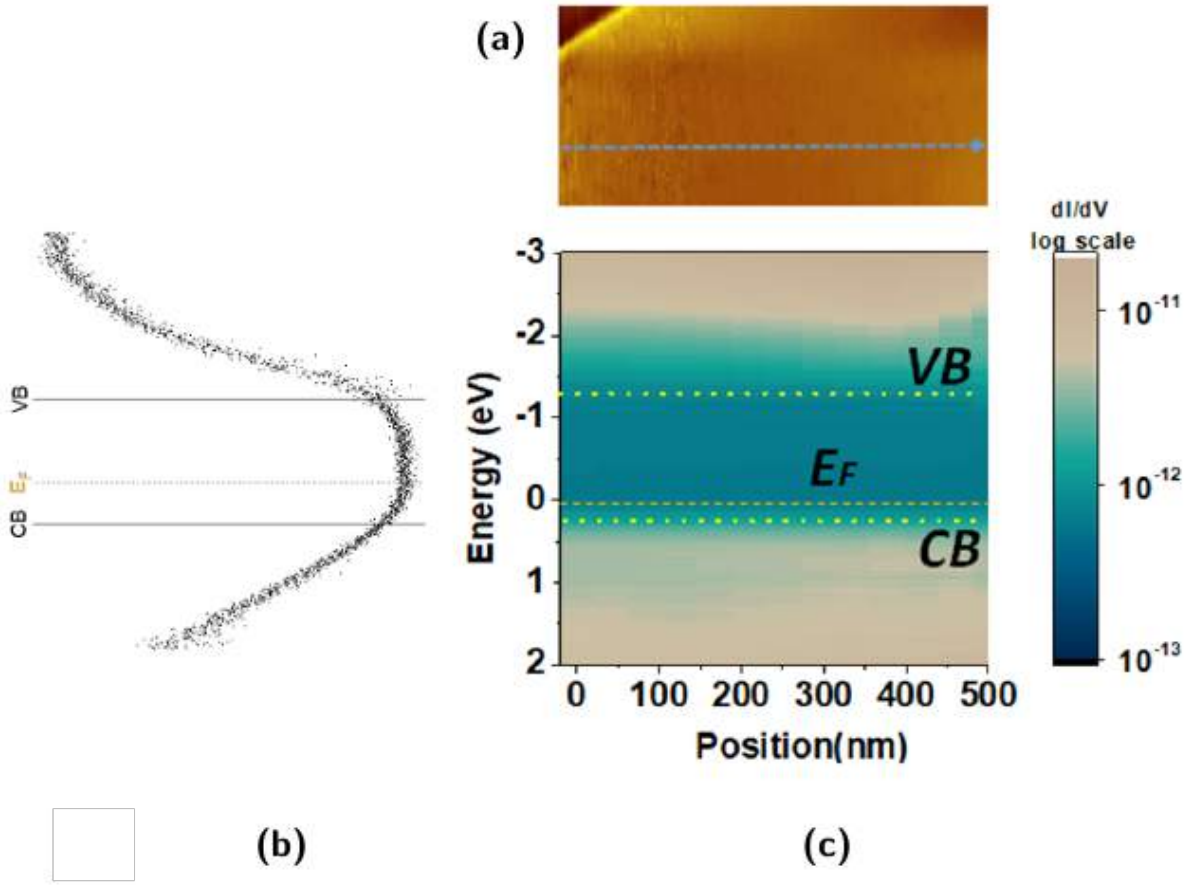

Figure 3.7: **(a)** Topography, with a 500nm line shown in blue representing the path of the conductance map. **(b)** The plot from Figure 3.5 is aligned sideways with the map to demonstrate the meaning of the plot. The intensity at any given point is the value dI/dV for a given position and energy. **(c)** Conductance map showing uniformity of spectra across a large area.

The position of the Fermi level and the valence and conduction bands do not vary significantly even across large areas in the crystal (Figure 3.7). Within our resolution, the Fermi level, valence band and conduction band are at the same point throughout these areas.

We also see that in areas with more defects, a feature appears in the gap near the valence side. Since this feature is associated with the presence of defects locally, it is not taken to be representative of the average band gap of ReS_2. For this reason, the value reported of $1.3 \pm 0.3eV$ does not include such spectra (Figure 3.8).

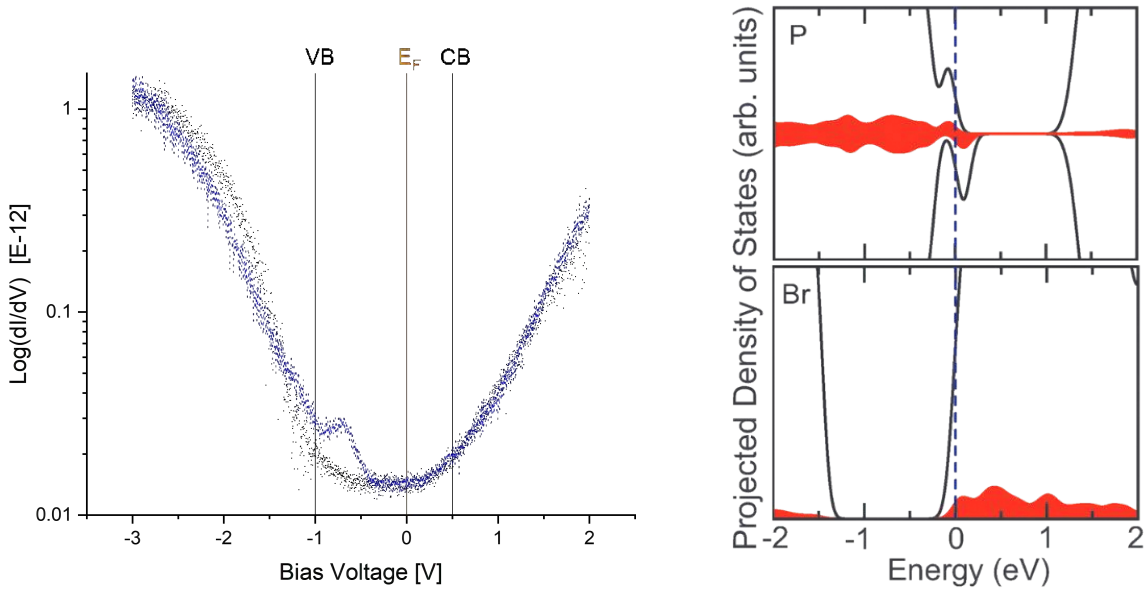

Figure 3.8: Defects in ReS_2 band structure. **(a)** Average of 64 ReS_2 spectra taken on a 20×20nm grid on areas with **(black)** no defects or **(blue)** defects. **(b)** DOS calculations[105] of P and Br substituted ReS_2. Red curve denotes partial DOS for the dopant atoms. The partial DOS for P is separated into spin up and spin down (plotted as negative DOS).

Defects. Impurities in the lattice can open up states within the band gap of the crystal, which will resemble surface states.[106] For negative bias, electrons tunnel from the occupied states in the tip to empty states of the surface, which can be empty states on the surface. On the other hand, when the tip is positively biased, they tunnel from valence band states of the sample to the tip, or from new states opened near the valence band edge, as we observed in Figure 3.8a. Furthermore, the defects in topographic scans reveal a polarity-dependent nature, appearing bright for negative tunneling bias (Figure 3.9a) and dark for positive bias (Figure 3.9b). The first condition likely represents the measurement of filled states near the valence band, of the kind which are observed in the STS data (Figure 3.8). The second represents tunneling into empty states. Similar observations have been reported on n-doped Si,[107] $PdSe_2$,[108] Mn-acceptors in GaAs,[109] and in other anisotropic crystals like BP.[110,111]

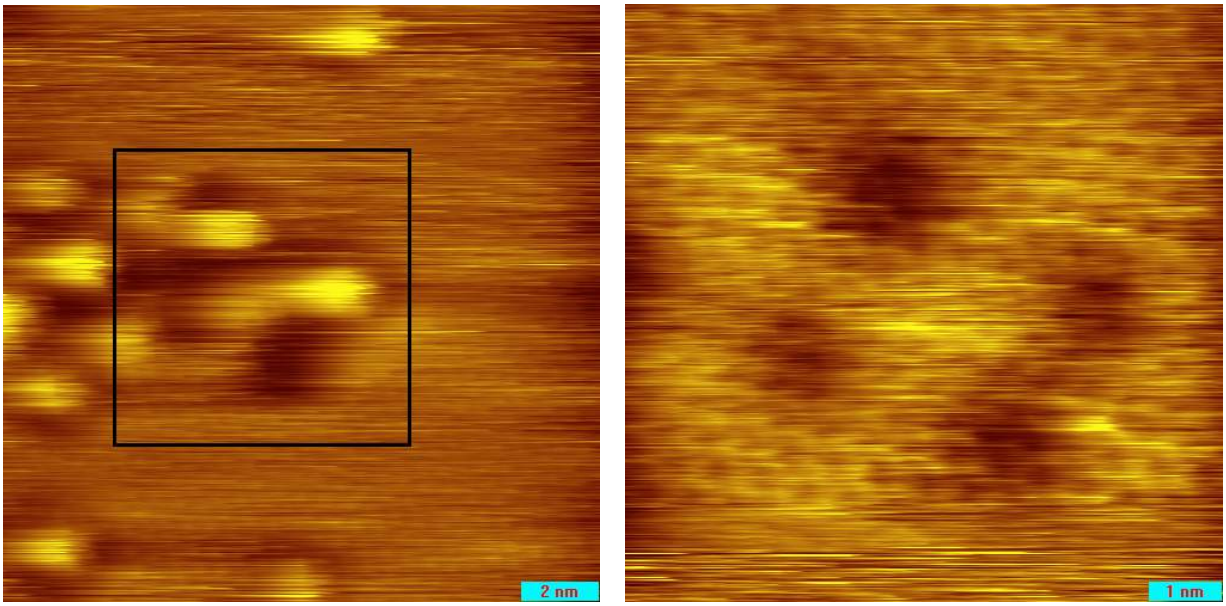

Figure 3.9: Representative images of defects in ReS_2 lattice. **(a)** Bright defects seen at negative bias voltage. V_b=-1.20V ; I_t=80pA. Size=15.6nm. Taken with RHK STM. **(b)** Zoom on black box from (a), showing dark defects with positive bias voltage. V_b=1.20V; I_t=80pA. Size=8.3nm. Taken with RHK STM.

With the smaller number of surface states accessed by STM, it is sensitive to the potential difference between the surface and tip, and is therefore susceptible to tip-induced band bending effects.[112–114] Such states cause a realignment of the bands relative to the surface state positions, which themselves are pinned to the Fermi level.[115] For n-type semiconductors, this effect induces an upwards curvature in the valence and conduction band edges at the surface. This bending effect arises naturally from chargeable surface states in the band gap present in the semiconductor-vacuum interface, but this interaction cannot be readily predicted because it depends on the local surface electronic structure and the shape of the tip.[114] It is in part a result of the restricted area in which the STM collects data.

The observed deviation of the valence and conduction band edges from flat band conditions in STS of ReS_2 is likely due to tip-induced band bending at the semiconductor-vacuum-metal interface.

By plotting local DOS maps at a given voltage, we can observe bright halos around defects. This supports the notion that they affect the local electrostatic environment, and this feature has been reported on surfaces of other layered 2D materials[108,110,111,116] as well as III-V semiconductors.[117–120] These are indicative of a TIBB effect, and this could be confirmed by measuring the relationship between the size of halos and the magnitude of the applied bias.[108,121]

3.2 Discussion

Measurements of terraces of ReS_2 confirm that the same anisotropic shape exhibited by exfoliated flakes is present on terraces of the bulk crystal. Our atomic resolution STM images corroborated previous reports of the lattice distortion of ReS_2,[80,83–86,96–100] and we concluded that the rhenium atoms were imaged here.

The measured local band gap of ReS_2 from STS agrees with values reported in literature.[45,78,79,79–85,85–87,87,90,101–103] The uniformity in the conductance maps (Figure 3.7) suggests that the shift in the Fermi level should be caused by the presence of defects locally, and by associated excess charge carriers. A large concentration of defects is indeed found on the surface of ReS_2, as can be seen in Figure 3.9.

While STM/STS do not offer chemical analysis, it is possible to hypothesize about the origin of the defects observed. Since the defect feature in the spectroscopy appears nearer to the valence edge of the band structure, it should be associated with electron acceptors (p-doping). It is possible that these are impurities from the growth process or Re/S vacancies in the lattice. Ref. [122] explored point defects in ReS_2 and indicated that S-substitutions require a lower formation energy, and should be arranged randomly in the crystal. Ref. [105] found similarly that B, N, P and As atoms substituting for S in the lattice would induce p-doping of ReS_2 monolayers, opening up defect states in the gap near the valence band edge. They add that Cl or Br substitutions would induce

ideal n-doping, donating their electrons directly to the conduction band of ReS_2.

While it is possible that some of the defects observed in the topography are B, N, P or As atoms(which would open up states in the band gap on the valence side), it is more likely that these are S vacancies in the lattice (which should have a similar effect). Both of these claims are supported by the spectroscopy data, in which the averaged data resembles the simulated DOS for Cl/Br, and spectroscopy focused on defects shows a state in the gap which most resembles the simulated DOS for P substitutions.

Some defects appear to remain bright despite changes in applied bias. The arguments presented in Ref.[108, 123], that the binding energy of donors might increase with proximity to the surface, could explain these observations, which were also reported in the study of n-doped Si.[107] It is also possible that two different types of defect are present, one of which has lower binding energy than the other (e.g. S vacancies for one type and Cl/Br substitutions for another).

Chapter 4

STM of the Atomic Lattice and CDW in 1T-TaS_2

TaS_2 is a TMDC with Tantalum (Ta) metal (group V) and Sulfur (S) chalcogen atoms. The crystals used in this thesis are in the 1T phase, but this material can also exist in a 2H phase. Both 1T- and 2H-TaS_2 have been shown to have superconducting states at temperatures below a few Kelvin.[124–126] A series of phase transitions in few-layer samples can be produced with 5 orders of magnitude of modulation in the resistance.[127] Below 350K, the crystal has a charge density wave (CDW) phase which is nearly commensurate (almost aligned) with the triangular lattice. If the material is cooled further (below 180K), an in-plane lattice distortion reorganizes tantalum atoms into "Star of David" clusters commensurate with the CDW (the center of each star coincides with the CDW).[124,126]

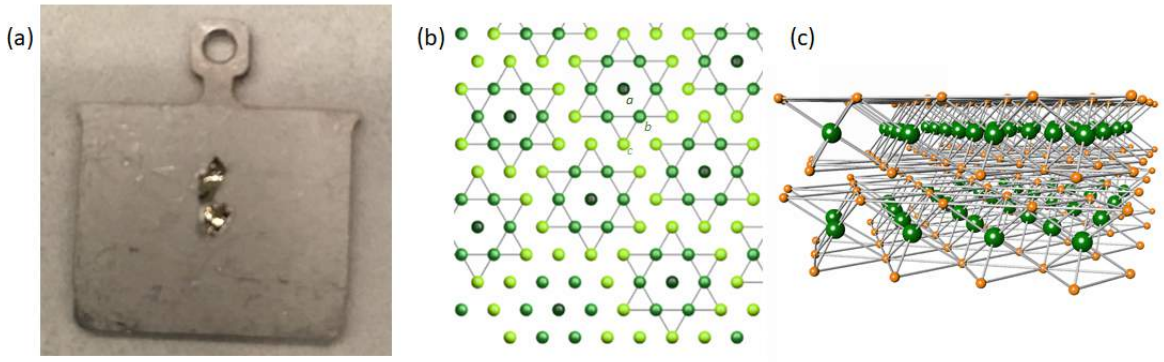

Figure 4.1: TaS_2 Crystal. **(a)** TaS_2 crystal on STM sample plate. **(b)** Top-down and **(c)** side view of TaS_2 lattice.

The top-down view of the lattice in Figure 4.1 shows this pattern, with different shades of green representing the Ta atoms within each star. The dark green atoms (denoted a) are aligned with the center of CDW modulations. The b and c atoms are the nearest and next-nearest neighbouring Ta atoms to the a atoms, and will have decreasing intensity in the STM images.

In this chapter, the surface of a 1T-TaS_2 crystal and its interaction with subsequently deposited TBrPP-Co molecules is examined. At the temperature that the experiment was performed (5K), 1T-TaS_2 enters a commensurate CDW phase, accompanied by the Star of David lattice deformation.

The 1T-TaS_2 crystal (HQ Graphene) was cleaved in air and immediately introduced in UHV. An image of the sample can be seen in Figure 4.1, attached to a sample plate with silver epoxy.

4.1 Results

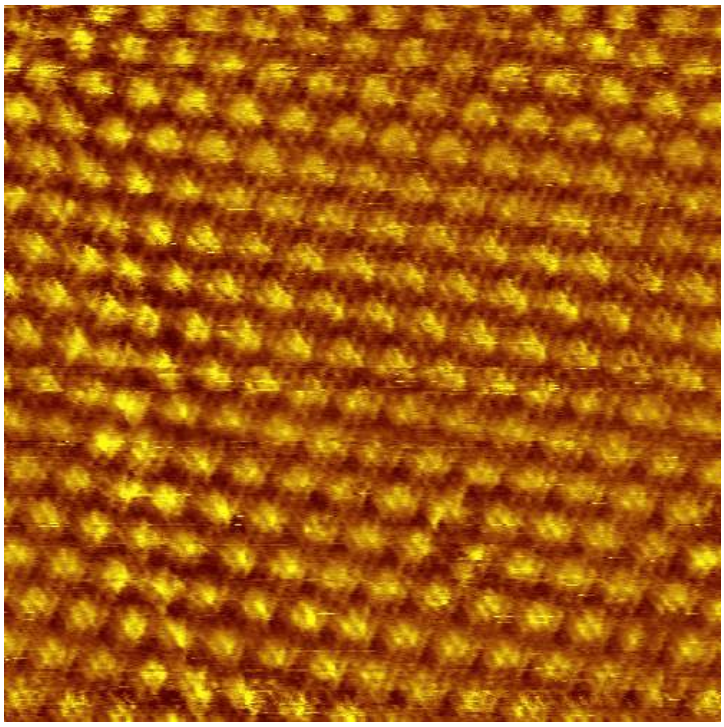

Figure 4.2: Representative STM topography of TaS_2 surface showing CDW. V_b=0.5V. I_t=450pA. Size=20nm. Taken with RHK STM.

Lattice observations were made to establish a baseline of the unaltered TaS_2 surface. It was typical to see the charge modulation (Figure 4.2a), but resolving the individual Ta atoms required particularly good tunneling conditions. An image visualizing both the CDW and the atoms within the same image can be seen in Figure 4.3c.

Similarly to ReS_2, measurements must be made here to confirm the type of atom imaged – in this case either Ta metal atoms or S chalcogen atoms. The in-plane Star of David lattice deformation is used as a reference point for measurements, as the center of CDW intensities aligns with the center of the stars. Two measurements must be made here. From the central Ta atom (a) within a star to its nearest neighbour (b), the measurements indicate a distance of $a_0 = 0.31 \pm 0.05$ nm. The commensurate CDW

in TaS_2 appears in STM as a $\sqrt{13} \times \sqrt{13}$ triangular superlattice with an angle of 120°, overlaid on the Ta lattice. Thus we expect distances of $\sqrt{13}a_0$ between CDWs. The distances from the center of neighbouring CDW peaks is measured to be 1.10 ± 0.06 nm, or $\sqrt{13}(0.31 \pm 0.02)$ nm. These values indicate that as expected, Ta atoms with an overlaid CDW are observed here.

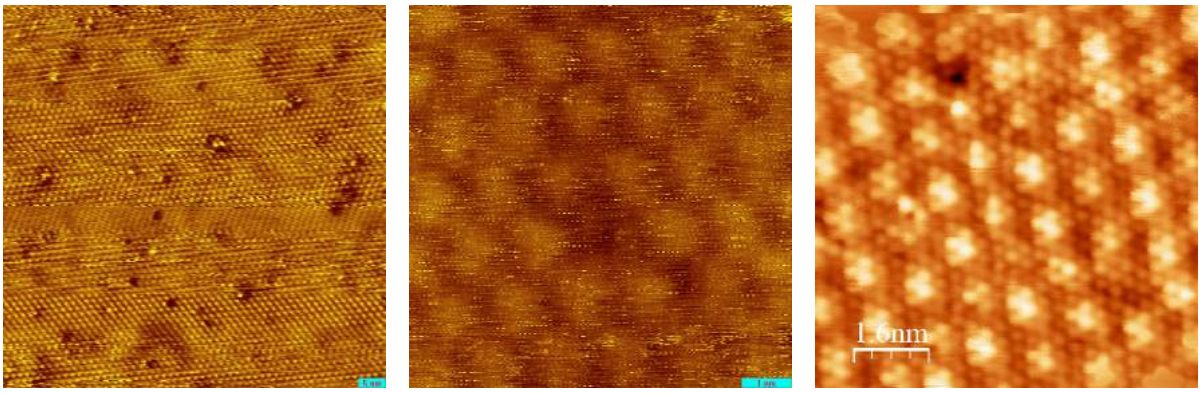

Figure 4.3: **(a)** Large-scale topography showing a variety of defects in TaS_2. V_b=0.5V. I_t=300pA. Size=70nm. Taken with RHK STM. **(b)** A "missing" CDW. V_b=0.5V. I_t=155pA. Size=7.5nm. Taken with RHK STM. **(c)** A vacancy in the top of the image near CDW modulations. V_b=1.0V. I_t=3nA. Size=8nm. Taken with homebuilt Createc STM.

Defects. During scanning, a variety of defects could be seen in the crystal. These included missing atoms and CDWs (4.3a, 4.3b), and domain walls (4.4). Often, atomic vacancies were associated with nearby modulations of the CDW pattern (Figures 4.3 and 4.4a), where the center of the CDW is not aligned with a single Ta atom.

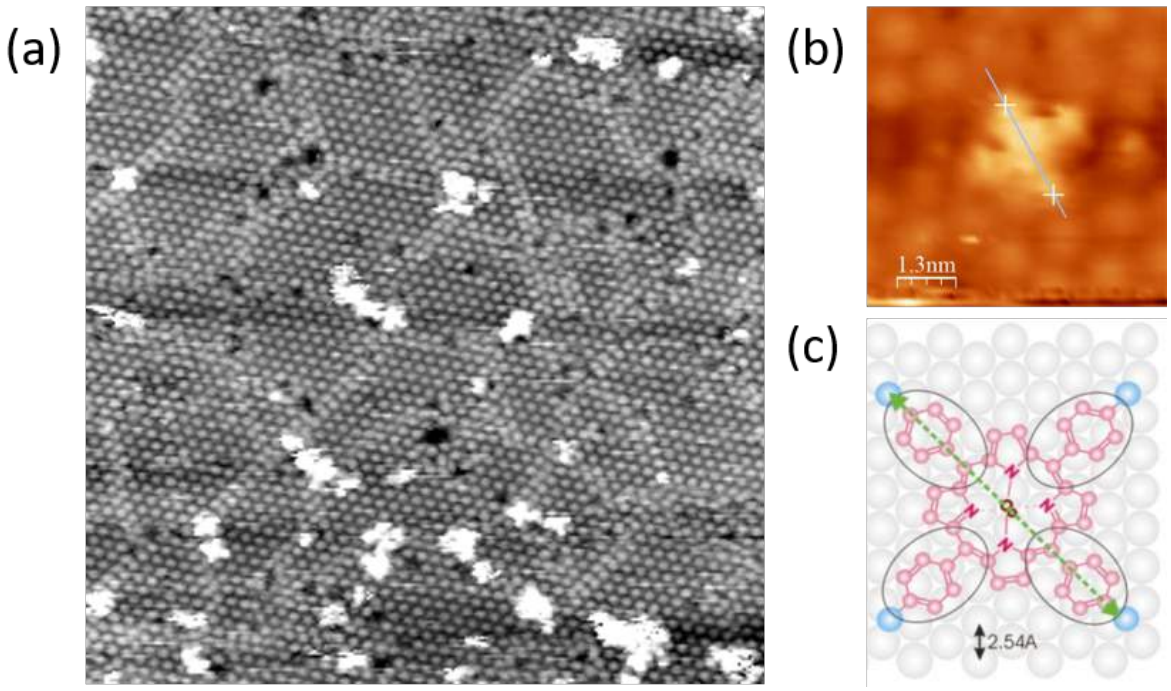

Figure 4.4: STM of TaS_2 with TBrPP-Co molecules (bright white spots) – taken with homebuilt Createc STM at Argonne National Labs. **(a)** TaS_2 with several molecules on the surface. V_b=2.75V. I_t=27pA. Size=60nm. **(b)** Single TBrPP-Co molecule on 1T-TaS_2. V_b=3.0V ; I_t=220pA. Size=6nm. **(c)** Representative image of TBrPP-Co molecule.

Molecules of magnetic TBrPP-Co were deposited onto the TaS_2 crystal by vaporization (120s at 310C).

The molecules were physisorbed onto the surface and therefore highly mobile during STM scanning, even at low temperatures. This poses a challenge for scanning tunneling spectroscopy, where the features being studied must remain stable for extended periods of time. In this regard, progress was made by developing a procedure for reliably finding and imaging these molecules on the surface.

During imaging, streaks in the STM topography were taken as a sign of molecules being pushed or dragged by the tip. Once resolved, larger groups of molecules appeared as bright clumps and tended to move a large distance between each scan. The system

was left to scan the same area repeatedly, which we assumed would move larger groups of molecules away, leaving only a few isolated molecules. The best images of CDW together with molecules were taken with a current of $2.0x10^{-11}A$ and a bias voltage of $2.65V$ (Figure 4.4). At lower bias (e.g. $0.5V$), only the CDW is visible, albeit with poor resolution. This is probably because the tip is closer to the surface and is able to push molecules away while scanning.

To confirm these were TBrPP-Co molecules they were measured diagonally – Figure 4.4 shows an example of this. According to [128], the diagonal lengths of the molecules in saddle or planar conformation (represented by the green line in Figure 4.4) are both $2.19nm$. By measuring a total of 14 isolated molecules, we found an average diagonal length of $2.21nm$, which agrees well with the previous study.

Chapter 5

Conclusion and Future Work

In this thesis, STM results were presented on 2D materials, with the goal of characterizing the topography and spectroscopy at the atomic level. Two crystals were studied in this way - ReS_2 and 1T-TaS_2. An understanding of the parent crystal is helpful before moving to their monolayer counterparts. The focus here was on bulk crystals, despite much of the interest in these particular materials being in their isolated 2D forms.

ReS_2. The principal experiment in this thesis was the characterization of bulk ReS_2. These experiments were performed on systems calibrated with graphite. From this, the lattice parameters of ReS_2 were determined (a= $0.59 \pm 0.05nm$, b=$0.62 \pm 0.06nm$, γ= $119 \pm 6°$) and it was concluded that clusters of 4 rhenium atoms are observed in the topography. The measured values for the interatomic distances and lattice parameters agree with those from TEM or X-ray spectroscopy. STS was used to obtain a value of the band gap ($1.3 \pm 0.3eV$), which compared well with the optical values from literature ($1.5 \pm 0.1eV$). Defects introducing electron acceptor states into the crystal were found, but more work needs to be done to understand the type of defects seen here, as well as their effect on the local electrostatic environment at the surface.

TaS_2. A study on TaS_2 crystals was also presented. Measurements of the lattice parameters were presented. We also described a procedure for reproducibly finding and imaging TBrPP-Co molecules on the TaS_2 surface, which will be beneficial for further research involving scanning tunneling spectroscopy of this system. Using this method,

we observed an interaction between these molecules and defects in the crystal. The periodic CDW from TaS_2 combined with the magnetic TBrPP-Co molecules forms a useful system for investigating the properties of CDW systems.

Future Work. As presented in Section 1.1 of Chapter 1, the properties of 2D crystals are dramatically different when their dimensionality is reduced. As such, the logical extension of this work is to move towards the characterization of isolated 2D sheets of ReS_2 or 1T-TaS_2.

Having understood the lattice structure of bulk ReS_2, the first project following this work should be to examine the lattice of its monolayer(prepared as in 2.2.1). A more thorough inspection is required into the defects in the material, in which the distinction between bulk and monolayer samples could help. Elemental analysis could be helpful in this regard to identify possible dopant substitutions. Future STS work should study monolayer ReS_2 to compare the gap with bulk. More spectroscopy data should be taken to find the exact contribution of defects to electronic states, and chemical analysis on these crystals should be performed to verify the presence of possible impurities.

Moving beyond individual crystals, new structures can be made by vertically stacking flakes into so-called van der Waals heterostructures. By stacking for example graphene on ReS_2 or TaS_2, the in-plane periodic structures could be utilized as periodic potentials which may alter the hexagonal lattice, induce strain, or affect the electronic structure of graphene to open a band gap. Inspecting these heterostructures with STM will provide details on a much smaller scale than is available to optical analysis, which has been the dominant characterization technique for similar experiments.

Further extension of this work can be done by studying suspended samples - samples not connected to or influenced by substrates. In this way the statement of the entire crystal being a surface can be truly realized, with the entire surface exposed to vacuum in the STM. By eliminating the substrate, a more fundamental characterization can be

performed. Some efforts towards this have been done in the form of decoupled samples.[129] More direct experiments have involved transferring CVD graphene above TEM grids or onto nanostructures,[130,131] but these have been limited by vibration and are easy to puncture. Developing a method in which samples are both suspended and rigidly fixed in place would solve these issues.

Chapter 6

Appendices

6.1 Additional STM Systems used for some data

NRC - Omicron STM-1. In addition to the RHK system used in this thesis was a room temperature Omicron UHV STM-1 located at the National Research Council of Canada (NRC) in Ottawa (Figure 6.1). Additional modules were added for a variety of metrology purposes, but the research in this thesis was performed only in the STM chamber (Figure 6.1b). Field emission was performed in the system to estimate and improve the sharpness of W tips, which were either obtained commercially from Bruker or made using the setup described in 2.2.2. These tips had to be resistance welded (Figure 6.2) onto small tip holders. The electronics and software which control the STM were updated to use the MATRIX control system provided by Scienta Omicron.

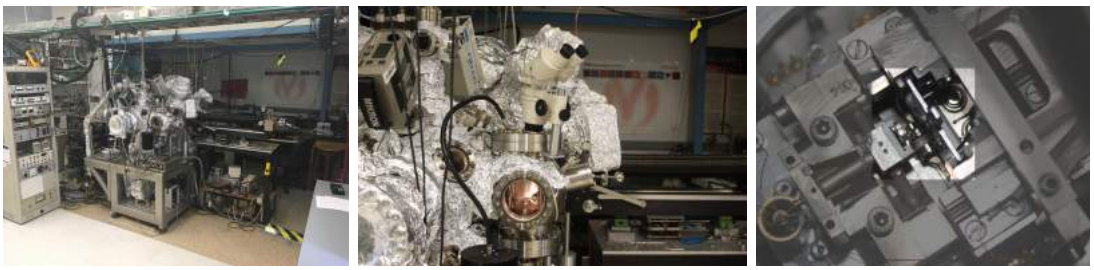

Figure 6.1: NRC's Omicron STM-1, STM chamber and scanning head. **(a)** Omicron STM-1. **(b)** STM chamber. **(c)** Scanning head with tip and sample highlighted.

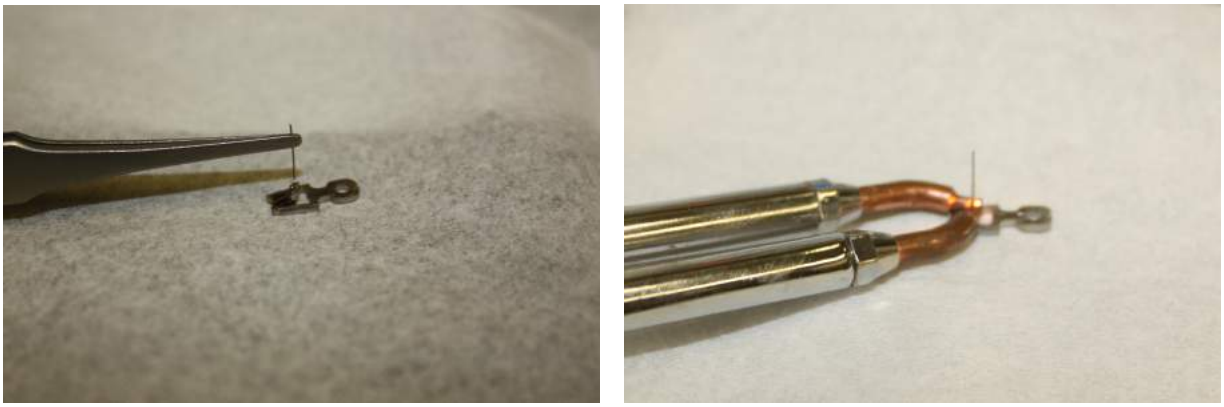

Figure 6.2: Resistance welding of tungsten tip in standard stm tip holder.

Figure 6.3: Argonne's homebuilt STM.

Argonne - homebuilt based on Createc. Some of the measurements from Chapter 4 were performed on an ultrahigh vacuum, low-temperature, homebuilt STM located at the Argonne National Labs in Chicago (Figure 6.3). For a full description, see reference [132]. The W tips used for the STM were affixed to q-plus cantilevers.

Low temperature was maintained with a two-bath system. This system is composed of an outer-wall containing liquid nitrogen, which acts as a shield for the inner wall, containing liquid helium. The sample chamber is in contact with this container, and the

sample is isolated from the rest of the system with metal gates. The temperature of the cryostat and STM are measured at all times, and the sample temperature is estimated from this to be around 5K when thermal equilibrium is reached.

Analysis on data received from all of the STMs was performed using both the Gwyddion and WSxM softwares, as well as the proprietary software associated with each system.

6.2 Complementary Material

Atomic force microscopy (AFM) and scanning electron microscopy (SEM) provided supplementary characterization. The AFM is a scanning probe technique, similar to STM, where the contrast is instead obtained from the force between the tip and sample. The AFM is used to confirm the thickness of samples and to check for surface contamination through topography and roughness measurements, respectively.

The SEM is often compared to an optical microscope, where a focused beam of electrons scan back and forth across the surface. The contrast here comes from electrons scattered off the surface — this can also give topographic information for our samples, but is primarily used to measure the sharpness of STM and AFM probes.

Figure 6.4: Scanning electron microscopes used for characterization and electron-beam lithography. **(a)** Gemini 500 SEM. **(b)** Raith Pioneer.

The Scanning Electron Microscope (SEM) was used for characterizing the sharpness of STM tips both before and after their use. It is was also used for electron-beam lithography (EBL) to pattern features onto substrates. In SEM, images are obtained by focusing a beam of electrons onto the sample and collecting scattered electrons.

The electron beam is emitted by an electron gun, and is focused onto the sample through an electron optics system. This system is used to deflect the beam such that the focal point is on the surface of the sample. The same electron optics system deflects the beam back and forth to raster scan across the surface, forming an image.

The electrons scattered by the sample lose some of their energy through absorption processes. This scattering can be either inelastic, producing secondary electrons reflected with energy lower than in the initial beam, or elastic, which produces high energy electrons. It is also possible for electromagnetic radiation to be produced. A specific type of detector must be used to measure the energy range associated with returning electrons from each of these processes. The positions and energies of these recaptured electrons are used to reconstruct the topography of the sample.

Images of tips taken by SEM can be seen in Figure 2.11.

The model used for basic metrology of tips was a GeminiSEM 500, seen in Figure 6.4a. The Raith Pioneer was the EBL tool used for patterning substrates. These systems both use standard tungsten tips, and operate under vacuum (below 10^{-9} Torr).

The Atomic Force Microscope (AFM) is a scanning probe technique similar to STM, but which uses a sharp tip on a cantilever to determine information about the morphology of a surface. The cantilever can oscillate and, depending on the method used, measure different properties from the surface. Rather than obtaining topographic information from tunneling current, AFM is sensitive to the attractive and repulsive forces between the sample and tip. It therefore lends itself to force measurements, where mechanical or electronic properties like the stiffness or resistivity are obtained. The use

of AFM in this thesis was to measure the topology of the samples to determine sample height and roughness. This information is used to infer the number of layers in 2D materials and the cleanliness of the surface.

A laser is focused on the end of the reflective tip, and its displacement is measured by a position sensitive photodetector. The tip raster scans across the surface and the frequency of oscillations (the force measured) changes in reaction to variations in the height of the surface. Similar to STM, a feedback loop keeps the frequency constant, and the amount it must be adjusted to remain at the correct level is used to determine the size of features it scanned over.

In non-contact AFM, images are obtained by oscillating a sharp tip just off its resonance frequency using a piezoelectric motor, around 100 nm above the surface of the sample. Contact and Tapping AFM use similar operating principles, but (as their names suggest) they are either in contact or repeatedly tapping the surface as they move along it. While typically giving greater resolution, the direct contact with samples poses a greater risk of sample destruction or contamination.

As AFM measurements are particularly sensitive, it is crucial to eliminate as much ambient noise as possible. For this reason, both of the AFMs used were contained in isolated acoustic enclosures on vibration isolating tables.

The particular models of AFMs used for these experiments were the Park NX10 and the Bruker Dimension Icon, seen in Figure 6.5. All images from these tools were obtained in air at room temperature. Data analysis was done using Park Systems' XEI software, as well as Gwyddion and WSxM.

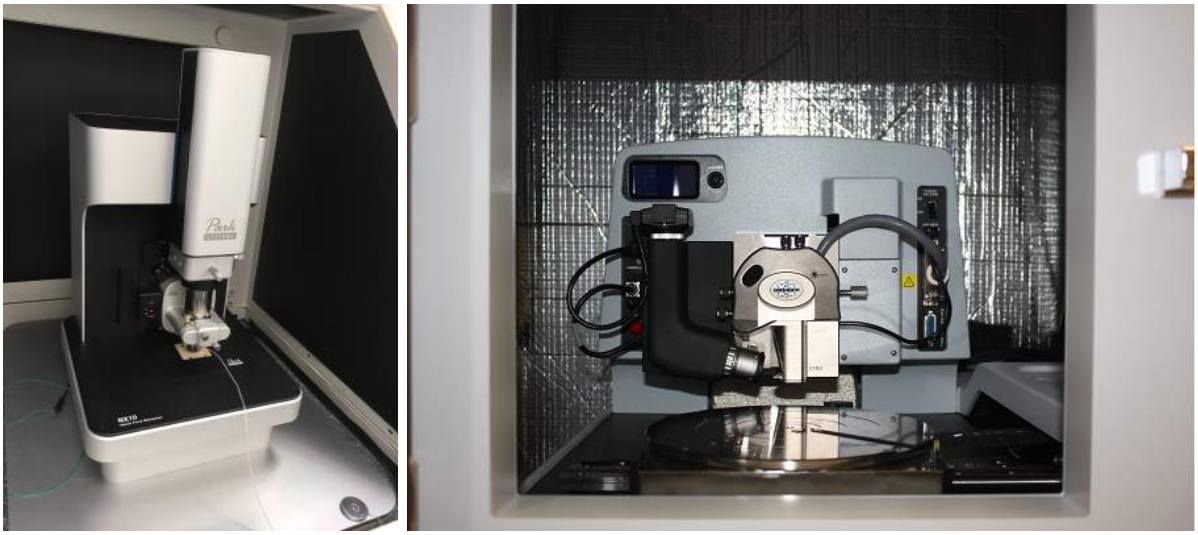

Figure 6.5: Atomic force microscopes. *Left:* Park NX10 AFM. *Right:* Bruker Dimension Icon AFM.

6.3 Tip Fabrication Through Electrochemical Etching

Tungsten wire (0.25 mm diameter) is etched at the interface of a NaOH solution in air through a one step electrochemical reaction,

$$W(s) + 2OH^- \longrightarrow WO_4^{2-} + 3H_2(g) \tag{6.1}$$

This reaction is utilized to shape the wire into a sharp, conical tip with apex radius typically less than 50nm (Figure 2.11). To achieve this, a circuit was constructed (Figure 2.12), in which the tungsten wire acts as an anode and a copper wire as a cathode.

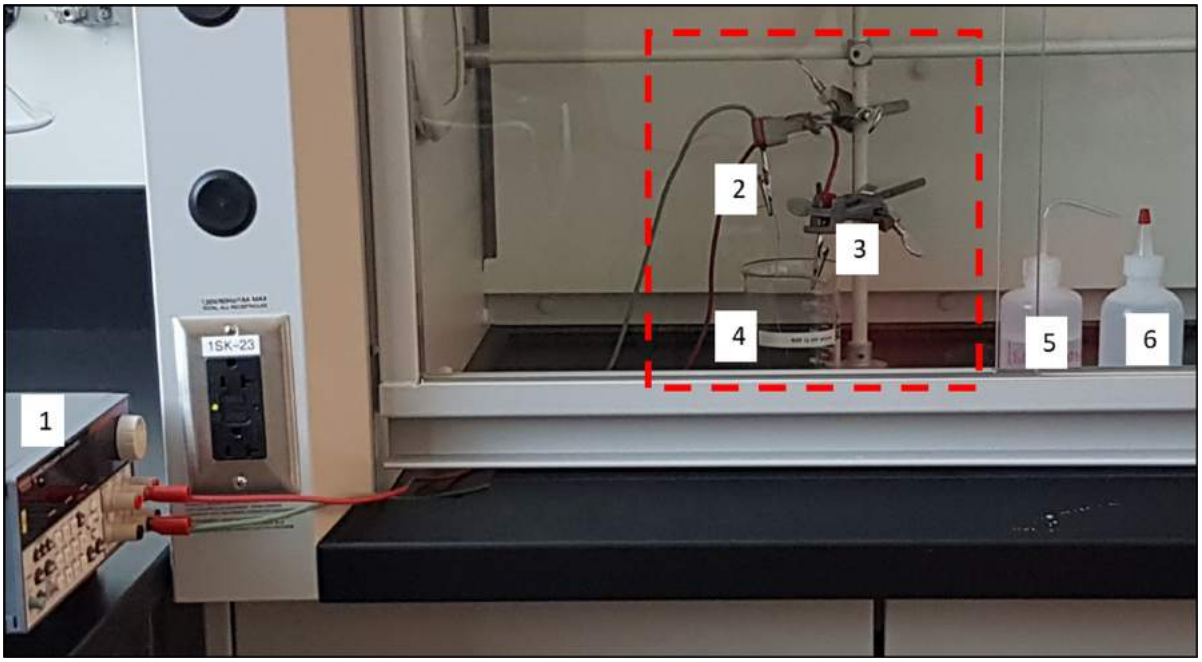

Figure 6.6: Full tip etching setup. As numbered, the components are: **(1)** Keithley power supply, **(2)** copper wire, **(3)** tungsten wire, **(4)** NaOH solution, **(5)** isopropanol and **(6)** distilled water.

Both wires are attached to a stand and one end of each wire is submerged in a solution of 2M NaOH (24g in 300mL distilled water). The copper wire should be well immersed in the solution in a ring geometry. This shape ensures the etching on the tungsten wire is symmetric.

The tungsten wire need only be submerged about 0.5 cm. The length determines the weight of the submerged portion – when the wire is too thin at the meniscus of the solution to support this weight, the submerged portion will detach. A smaller submerged portion increases the time for the reaction and improves the final tip radius that can be achieved.

The other ends of the wires are connected with alligator clips to a power supply (Keithley 2231A-30-3 DC). A voltage of 9 V and a current of approximately 18 mA results in a reaction time of approximately 15 minutes. The end of the reaction is

determined by a sudden drop of the current to zero, associated with the submerged W portion detaching. The wire is removed from the solution manually when the current is interrupted. Afterwards, the NaOH solution is cleaned off with isopropanol (IPA) and distilled water.

6.4 Tunneling Current Derivation

Before obtaining the reflection and transmission coefficients, we can make an assumption that particles are incident from $z < 0$, with an incident amplitude of A and a reflected amplitude of B. This simplifies the transmitted wave (in $z > d$) since there is nothing in $z > d$ to reflect particles. We can take $D = 0$ and simplify to:

$$\psi(z) = \begin{cases} Ae^{ikz} + Be^{-ikz}, & \text{if } z < 0. \\ Ce^{ikz}, & \text{if } z > d. \end{cases} \tag{6.2}$$

Now we can calculate $j(z,t)$, the probability current density.

$$j(z,t) = \frac{\hbar}{2mi}\Big[\psi^\dagger(z,t)\delta_z(\psi(z,t)) - \psi(z,t)\delta_z(\psi^\dagger(z,t))\Big] \tag{6.3}$$

$$j(z,t) = \begin{cases} \frac{\hbar k}{m}(|A|^2 - |B|^2), & \text{if } z < 0. \\ \frac{\hbar k}{m}|C|^2, & \text{if } z > d. \end{cases} \tag{6.4}$$

From this, two cases emerge: $E > V_0$ and $E < V_0$. The solution which is relevant to STM is $E < V_0$, as electrons in the sample and tip will have less energy than the potential barrier between these two regions. As such, the transmission coefficient that we find from this case will be equivalent to the tunneling current with a voltage applied.

With that in mind, we can define the reflection (R) and transmission (T) coefficients, given by the ratio of the reflected wave or the transmitted wave to the incident wave,

respectively:

$$R = \frac{|B|^2}{|A|^2} \qquad and \qquad T = \frac{|C|^2}{|A|^2} \tag{6.5}$$

and we can also define $K = \frac{1}{\hbar}(2m(V_0 - E))^{\frac{1}{2}}$ for $E < V_0$. The solution for Schrödinger's equation inside the potential is:

$$\psi(z) = Fe^{Kz} + Ge^{-Kz}, \quad 0 < z < d \tag{6.6}$$

Now that we have a solution both inside and outside the potential, we can relate them by requiring that both $\psi(z)$ and $\delta_z\psi(z)$ are continuous at $z = 0$ and $z = d$. This gives a system of equations:

$$\begin{aligned} A + B &= F + G \\ ik(A - B) &= K(F - G) \quad \text{at } z = 0, \\ Ce^{ikd} &= Fe^{Kd} + Ge^{-Kd} \\ ikCe^{ikd} &= K(Fe^{Kd} - Ge^{-Kd}) \quad \text{at } z = d \end{aligned} \tag{6.7}$$

Which can be solved to get R and T.

$$\begin{aligned} R &= \left[1 + \frac{4E(V_0 - E)}{(V_0)^2 sinh^2(Kd)}\right]^{-1} \\ T &= \left[1 + \frac{(V_0)^2 sinh^2(Kd)}{4E(V_0 - E)}\right]^{-1} \end{aligned} \tag{6.8}$$

We see that T approaches zero in the limit of E going to zero and that it scales monotonically with E. In fact, if $Kd \gg 1$, then $sinh(Kd) \approx \frac{1}{2}e^{Kd}$, and we can substitute this

into T in equation 6.8:

$$T = \frac{1}{1 + \frac{V_0^2}{16E(V_0-E)}e^{2Kd}} = \frac{\left[\frac{16E(V_0-E)}{V_0^2 e^{2Kd}}\right]}{\left[\frac{16E(V_0-E)}{V_0^2 e^{2Kd}}\right] + 1} \tag{6.9}$$

Considering that the portion in the square brackets is very small, the denominator can be approximated as equal to 1. Thus:

$$T \approx \frac{16E(V_0-E)}{V_0^2}e^{-2Kd} \tag{6.10}$$

which corresponds to the amount of current which is transmitted, that is, the tunneling current we measure in STM:

$$I_t \propto e^{-2Kd} \tag{6.11}$$

6.5 Manual Calculation of the Calibration Factors

We must first determine the lattice vectors on our image, the procedure for which is the same as in Chapter 2.2.3. The measured values for the a and b vectors on the image are 2×1 matrices, separated by an angle ϕ:

$$\vec{a} = \begin{pmatrix} a_x \\ a_y \end{pmatrix}, \quad \vec{b} = \begin{pmatrix} b_x \\ b_y \end{pmatrix}, \qquad \phi = \cos^{-1}\left(\frac{\vec{a}\cdot\vec{b}}{|\vec{a}||\vec{b}|}\right) \tag{6.12}$$

We will apply a 2×2 affine transformation matrix **A** to the vectors to correct them. This matrix is a combination of three 2×2 matrices. The matrix **R** is applied first to rotate the vectors such that $\vec{a}$ is aligned with the x-axis. Then **C** is a scaling matrix, which corrects the magnitudes of $\vec{a}$ and $\vec{b}$ to some known value L. Finally, **S** applies a shear

(or skew) to correct the angle between the vectors.

$$\mathbf{R} = \begin{bmatrix} \cos\theta & \sin\theta \\ -\sin\theta & \cos\theta \end{bmatrix}, \qquad \mathbf{C} = \begin{bmatrix} c_x & 0 \\ 0 & c_y \end{bmatrix}, \qquad \mathbf{S} = \begin{bmatrix} 1 & \tan(\phi-\gamma) \\ 0 & 1 \end{bmatrix} \tag{6.13}$$

$$\mathbf{A} = \mathbf{S}\ \mathbf{C}\ \mathbf{R}$$

We will have to define what θ, c_x, c_y, and γ are as we proceed.

For $\mathbf{R}$, we would like to rotate our axes such that the y-component of $\vec{a}$ is zero. The motivation behind this is so that $\mathbf{S}\vec{a} = \vec{a}$, because this matrix applies a shear based on the y-component of the vectors. Thus we will only have to consider the effect of $\mathbf{S}$ on $\vec{b}$. So the angle θ (which in practice is determined when $\vec{a}$ is measured) is just the angle of $\vec{a}$ from the x-axis, or:

$$\theta = \cos^{-1}\left(\frac{a_x}{|\vec{a}|}\right) \tag{6.14}$$

Now we would like to scale our vectors. To determine c_x and c_y, we must compare the magnitude of $\vec{a}$ and $\vec{b}$ to the theoretical lattice parameters. The rotation of $\vec{a}$ makes it easy to find c_x:

$$c_x = \frac{L}{|\vec{a}|} = \frac{L}{a_x} \tag{6.15}$$

where L is the correct length of the lattice parameters. This correction is easily applied to $\vec{a}$:

$$\vec{a'} = \begin{bmatrix} c_x & 0 \\ 0 & c_y \end{bmatrix} \vec{a} = \begin{pmatrix} c_x a_x \\ 0 \end{pmatrix} = \begin{pmatrix} L \\ 0 \end{pmatrix} \tag{6.16}$$

Now we will find c_y, and it should become evident why the symmetry of graphite is helpful for calibration, as we require that the correct lattice parameters have the same magnitude $|\vec{a}| = |\vec{b}| = L$. First, we apply $\mathbf{C}$ to $\vec{b}$:

$$\begin{aligned}\begin{bmatrix} c_x & 0 \\ 0 & c_y \end{bmatrix} \begin{pmatrix} b_x \\ b_y \end{pmatrix} &= \begin{pmatrix} c_x b_x \\ c_y b_y \end{pmatrix} \\ &= \begin{pmatrix} \frac{L}{a_x} b_x \\ c_y b_y \end{pmatrix}\end{aligned} \tag{6.17}$$

$$|\vec{b'}| = \sqrt{\Big(\frac{L}{a_x} b_x\Big)^2 + (c_y b_y)^2}$$

then compare the magnitudes of $\vec{b'}$ and $\vec{L}$ to solve for c_y:

$$1 = \frac{|\vec{b'}|}{|\vec{L}|} = \frac{\sqrt{\Big(\frac{L}{a_x} b_x\Big)^2 + (c_y b_y)^2}}{\sqrt{L^2}}$$

$$\begin{aligned} L &= \sqrt{\Big(\frac{L}{a_x} b_x\Big)^2 + (c_y b_y)^2} \\ L^2 &= \frac{L^2}{a_x^2} b_x^2 + c_y^2 b_y^2 \\ c_y &= \frac{L}{b_y}\Big(1 - \frac{b_x^2}{a_x^2}\Big)^{\frac{1}{2}} \end{aligned} \tag{6.18}$$

We now have expressions for c_x and c_y, both of which depend on only the measured vectors and the (known) correct lattice parameters.

Finally, the skew matrix can be applied to correct the angle between the vectors. In principle, one need only apply it along either the x- or y-axis to correct the image. The skew matrix $\mathbf{S}$ does not preserve magnitudes, but by changing our coordinates we ensure that only $\vec{b'}$ will be affected.

The shearing factor is determined from the angle ϕ between the vectors $\vec{a}$ and $\vec{b'}$, and the correct angle γ. For example in graphite, $\gamma = 60°$. When applied to the corrected $\vec{b}$, we get:

$$\begin{bmatrix} 1 & \tan(\phi - \gamma) \\ 0 & 1 \end{bmatrix} \begin{pmatrix} c_x b_x \\ c_y b_y \end{pmatrix} = \begin{pmatrix} c_x b_x + c_y b_y \tan(\phi - \gamma) \\ c_y b_y \end{pmatrix} \tag{6.19}$$

This skewing matrix corrects $\vec{b}$ by changing its x-component. This will change the dot product between $\vec{a'}$ and $\vec{b'}$, and the result can be visualized as a "rotation" towards $\vec{a}$ by an angle $\phi - \gamma$. Since this is explicitly the difference between the measured and the correct angle, the matrix moves $\vec{b}$ to this correct angle γ.

As a result of changing only one coordinate in $\vec{b}$, the magnitude has now changed by a small amount. We can then compare the magnitude of $\vec{b}$ to L to correct both components by the same factor, just as we did to get c_x. At this point, we will have two vectors with exactly the correct magnitudes, separated by an angle very close to the correct value. The desired level of precision can be obtained by repeating this procedure, with each successive application converging closer to the real parameters. We can give the correction factors we determined from this procedure to the STM software to calibrate it, or we can apply this correction manually to images taken after this calibration.

Bibliography

[1] W. Melitz et al. Band offsets in semiconductor heterojunctions. 2010.

[2] K. S. Novoselov, A. K. Geim, S. V. Morozov, D. Jiang, Y. Zhang, S. V. Dubonos, I. V. Grigorieva, and A. A. Firsov. Electric field effect in atomically thin carbon films. *Science*, 306(5696):666–669, 2004.

[3] A. K. Geim. Graphene: Status and prospects. *Science*, 324(5934):1530–1534, 2009.

[4] A.K. Geim and K.S. Novoselov. The rise of graphene. *Nature Materials*, 6:183–191, 2007.

[5] K. S. Novoselov, D. Jiang, F. Schedin, T. J. Booth, V. V. Khotkevich, S. V. Morozov, and A. K. Geim. Two-dimensional atomic crystals. 102(30):10451–10453, 2005.

[6] Alexander A. Balandin, Suchismita Ghosh, Wenzhong Bao, Irene Calizo, Desalegne Teweldebrhan, Feng Miao, and Chun Ning Lau. Superior thermal conductivity of single-layer graphene. *Nano Letters*, 8(3):902–907, 2008. PMID: 18284217.

[7] R. R. Nair, P. Blake, A. N. Grigorenko, K. S. Novoselov, T. J. Booth, T. Stauber, N. M. R. Peres, and A. K. Geim. Fine structure constant defines visual transparency of graphene. *Science*, 320(5881):1308–1308, 2008.

[8] Y. Cao et al. Unconventional superconductivity in magic-angle graphene superlattices. *Nature*, 556:43–50, 2018.

[9] G. R. Stewart. Unconventional superconductivity. *Advances in Physics*, 66:75–196, 2017.

[10] M. Norman. The Challenge of Unconventional superconductivity. *Science*, 332:196–200, 2011.

[11] A. Gurevich. To use or not to use cool superconductors? *Nature Materials*, 10:255–259, 2011.

[12] R. Dong and I. Kuljanishvili. Review Article: Progress in fabrication of transition metal dichalcogenides heterostructure systems. *J Vac Sci Technol B Nanotechnol Microelectron.*, 35:030803, 2017.

[13] J. A. Wilson and A. D. Yoffe. The transition metal dichalcogenides discussion and interpretation of the observed optical, electrical and structural properties. *Advances in Physics*, 18:193–335, May 1969.

[14] N. V. Podberezskaya, S. A. Magarill, N. V. Pervukhina, and S. V. Borisov. Crystal chemistry of dichalcogenides mx_2. *Journal of Structural Chemistry*, 42:654–681, 2001.

[15] M. Chhowalla, Shin, H. S., G. Eda, L.-J. Li, and H. Loh, K. P. andZhang. The chemistry of two-dimensional layered transition metal dichalcogenide nanosheets. *Nature Chemistry*, 5:263–275, 2013.

[16] A. H. Castro Neto. Charge density wave, superconductivity, and anomalous metallic behavior in 2d transition metal dichalcogenides. *Phys. Rev. Lett.*, 86:4382–4385, May 2001.

[17] D. Jariwala, V. Sangwan, L. Lauhon, T. Marks, and M. Hersam. Emerging device applications for semiconducting two-dimensional transition metal dichalcogenides. *ACS Nano*, pages 1102–1120, 2014.

[18] Kin Fai Mak, Changgu Lee, James Hone, Jie Shan, and Tony F. Heinz. Atomically thin mos_2: A new direct-gap semiconductor. *Phys. Rev. Lett.*, 105:136805, Sep 2010.

[19] W. Jin et al. Direct measurement of the thickness-dependent electronic band structure of mos_2 using angle-resolved photoemission spectroscopy. *Phys. Rev. Lett.*, 111:106801, 2013.

[20] L. Yang, N. Sinitsyn, W. Chen, J. Yuan, J. Zhang, J. Lou, and S. Crooker. Why all the fuss about 2d semiconductors? *Nature Photonics*, page 202–204, 2016.

[21] Di Xiao, Gui-Bin Liu, Wanxiang Feng, Xiaodong Xu, and Wang Yao. Coupled spin and valley physics in monolayers of mos_2 and other group-vi dichalcogenides. *Phys. Rev. Lett.*, 108:196802, May 2012.

[22] Y. Ziliang, C. Ting, K. O'Brien, Z. Hanyu, Y. Xiaobo, W. Yuan, Steven L. G., and Z. Xiang. Probing excitonic dark states in single-layer tungsten disulphide. *Nature*, 513, 2014.

[23] B. Mohanty, M. Ghorbani-Asl, S. Kretschmer, A. Ghosh, P. Guha, S. K. Panda, B. Jena, A. V. Krasheninnikov, and B. K. Jena. Mos_2 quantum dots as efficient catalyst materials for the oxygen evolution reaction. *ACS Catalysis*, 8(3):1683–1689, 2018.

[24] Q. Fanyao, A. C. Dias, J. Fu, L. Villegas-Lelovsky, and D. L. Azevedo. Tunable spin and valley dependent magneto-optical absorption in molybdenum disulfide quantum dots. *Scientific Reports*, 7:41044, 2017.

[25] R. Pisoni, Z. Lei, P. Back, M. Eich, H. Overweg, Y. Lee, K. Watanabe, T. Taniguchi, T. Ihn, and K. Ensslin. Gate-tunable quantum dot in a high quality single layer mos_2 van der Waals heterostructure. *Appl. Phys. Lett.*, 112:123101, 2018.

[26] C. Schneider, M. Glazov, T. Korn, S. Höfling, and B. Urbaszek. Two-dimensional semiconductors in the regime of strong light-matter coupling. *Nature Communications*, page 2695, 2018.

[27] G. Plechinger, P. Nagler, A. Arora, R. Schmidt, A. Chernikov, A. del Águila, P. Christianen, R. Bratschitsch, C. Schüller, and T. Korn. Trion fine structure and coupled spin–valley dynamics in monolayer tungsten disulfide? *Nature*, page 12715, 2016.

[28] G. Wang, L. Bouet, D. Lagarde, M. Vidal, A. Balocchi, T. Amand, X. Marie, and B. Urbaszek. Valley dynamics probed through charged and neutral exciton emission in monolayer wse_2. *Phys. Rev. B*, 90:075413, Aug 2014.

[29] L. Yang, N. Sinitsyn, W. Chen, J. Yuan, J. Zhang, J. Lou, and S. Crooker. Long-lived nanosecond spin relaxation and spin coherence of electrons in monolayer mos_2 and ws_2. *Nature*, 2015.

[30] B. Radisavljevic, A. Radenovic, J. Brivio, V. Giacometti, and A. Kis. Single-layer mos_2 transistors. *Nature Nanotechnology*, pages 147–150, 2011.

[31] F. Schwierz, J. Pezoldt, and R. Granzner. Two-dimensional materials and their prospects in transistor electronics. *Nanoscale*, 7:8261–8283, 2015.

[32] H. Li, Y. Shi, M. H. Chiu, and L. Li. Emerging energy applications of two-dimensional layered transition metal dichalcogenides. 18, 10 2015.

[33] W. Choi et al. High-detectivity multilayer mos_2 phototransistors with spectral response from ultraviolet to infrared. *Adv. Mater.*, pages 5832–5836, 2012.

[34] Z. Yin, H. Li, H. Li, L. Jiang, Y. Shi, Y. Sun, G. Lu, Q. Zhang, X. Chen, and H. Zhang. Single-layer mos_2 phototransistors. *ACS Nano*, pages 74–80, 2012.

[35] W. J. Yu, Y. Liu, H. Zhou, A. Yin, Z. Li, Y. Huang, and X. Duan. Highly efficient gate-tunable photocurrent generation in vertical heterostructures of layered materials. *Nat. Nanotechnol.*, page 952–958, 2013.

[36] V. K.; Wu C.-C.; Prabhumirashi P. L.; Geier M. L.; Marks T. J.; Lauhon L. J.; Hersam M. C. Jariwala, D.; Sangwan. Gate-tunable carbon nanotube–mos_2 heterojunction p-n diode. *Proc. Natl. Acad. Sci. U.S.A.*, page 18076–18080, 2013.

[37] M. Bernardi, M. Palummo, and J. C. Grossman. Extraordinary sunlight absorption and one nanometer thick photovoltaics using two-dimensional monolayer materials. *Nano Lett.*, pages 3664–3670, 2013.

[38] A. Pospischil, M. M. Furchi, and T. Mueller. Solar energy conversion and light emission in an atomic monolayer p-n diode. *Nature Nanotechnology*, page 257–261, 2013.

[39] J. Feng, X. Qian, C.-W. Huang, and J. Li. Strain-engineered artificial atom as a broad spectrum solar energy funnel. *Nat. Photon.*, pages 866–872, 2012.

[40] Y. Y. Hui, X. Liu, W. Jie, N. Y. Chan, J. Hao, Y.-T. Hsu, L.-J. Li, W. Guo, and S. P. Lau. Exceptional tunability of band energy in a compressively strained trilayer mos_2 sheet. *ACS Nano*, pages 7126–7131, 2013.

[41] S. Tongay, J. Zhou, C. Ataca, J. Liu, J. S. Kang, T. S. Matthews, L. You, J. Li, J. C. Grossman, and J. Wu. Broad-range modulation of light emission in two-dimensional semiconductors by molecular physisorption gating. *Nano Lett.*, pages 2831–2836, 2013.

[42] J. Tao, W. Shen, S. Wu, L. Liu, Z. Feng, C. Wang, C. Hu, P. Yao, H. Zhang, W. Pang, X. Duan, J. Liu, C. Zhou, and D. Zhang. Mechanical and electrical anisotropy of few-layer black phosphorus. *ACS Nano*, 9(11):11362–11370, 2015.

[43] P. A. D. Goncalves, S. Xiao, and N. M. R. Peres. Hybridized plasmons in 2d nano-slits: From graphene to anisotropic 2d materials. *ACS Photonics*, 4, 2017.

[44] A. Brown and S. Rundqvist. Refinement of the crystal structure of black phosphorus. *Acta Cryst.*, 19:684–685, 1965.

[45] H. X. Zhong et al. Quasiparticle band gaps, excitonic effects, and anisotropic optical properties of the monolayer distorted 1T diamond-chain structures ReS_2 and $ReSe_2$. *Physical Review B.*, 92, 2015.

[46] Invisible growth of microstructural defects in graphene chemical vapor deposition on copper foil", journal = Carbon, volume = 96, pages = 237 - 242, year = 2016, issn = 0008-6223, doi = https://doi.org/10.1016/j.carbon.2015.09.041, url = http://www.sciencedirect.com/science/article/pii/S0008622315302608, author = Yanhui, Z. and Haoran, Z. and Feng, L. and Haibo, S. and Zhiying, C. and Yanping, S. and Yaqian, Z. and Xiaoming, G. and Guanghui, Y. and Zhi, J. and Xinyu, L. .

[47] L. Colombo, B. Li, X. Han, C. Magnuson, W. Cai, Y. Zhu, and R. Ruoff. Growth kinetics and defects of cvd graphene on cu. *ECS Trans.*, 28(5):109–114, 2010.

[48] O. Cretu, Y.-C. Lin, and K. Suenaga. Evidence for active atomic defects in monolayer hexagonal boron nitride: A new mechanism of plasticity in two-dimensional materials. *Nano Letters*, 14(2):1064–1068, 2014.

[49] Z. Cai, B. Liu, X. Zou, and H.-M. Cheng. Chemical vapor deposition growth and applications of two-dimensional materials and their heterostructures. *Chemical Reviews*, 118(13):6091–6133, 2018.

[50] The nobel prize in physics 1986. *Nobel Media AB*, 2018.

[51] B. H. Bransden and C. J. Joachain. *Quantum Mechanics*. Pearson, 2000.

[52] J. Bardeen. Tunnelling from a Many-Particle Point of View. *Physical Review Letters*, 6:57, 1961.

[53] P. Albrecht, K. Ritter, and L. Ruppalt. The bardeen transfer hamiltonian approach to tunneling and its application to stm and carbon nanotubes, 2004.

[54] J. C. Chen. *Introduction to Scanning Tunneling Microscopy*. Oxford University Press, 1993.

[55] L. D. Landau and E. M. Lifshitz. *Quantum Mechanics Non-Relativistic Theory*. Pergamon Press, Oxford, 1977.

[56] J. Tersoff and D. R. Hamann. Theory and Application for the scanning tunneling microscope. *Phys. Rev. B.*, 50:1998, 1983.

[57] J. Tersoff and D. R. Hamann. Theory of the scanning tunneling microscope. *Phys. Rev. B.*, 31:805, 1985.

[58] Roland Wiesendanger. *Scanning Probe Microscopy and Spectroscopy: Methods and Applications*. Cambridge University Press, 1994.

[59] J. A. Stroscio and W. J. Kaiser. *Scanning Tunneling Microscopy*. Acadaemic Press, 1993.

[60] C. J. Chen. *Introduction to Scanning Tunneling Microscopy*. Oxford University Press, 1993.

[61] M. S. Chung, T. E. Feuchtwang, and P. H. Cutler. Spherical Tip Model in the Theory of the Scanning Tunneling Microscope. *Surface Science*, 187:559, 1987.

[62] C.. J. Chen. Theory of scanning tunneling spectroscopy. *J. of Vac. Sci. Tech.*, 6:319, 1988.

[63] C.. J. Chen. Origin of atomic resolution on metal surfaces in scanning tunneling microscopy. *Phys. Rev. Lett.*, 64:448, 1990.

[64] J. Tersoff. Role of tip electronic structure in scanning tunneling microscope images. *Phys. Rev. B.*, 41:1235, 1990.

[65] S. G. Jennings. The mean free path in air. *Journal of Aerosol Science*, 19:159–166, 1988.

[66] D. E. Allen and G. Pernica. Control of Floor Vibration, 1998.

[67] O. Hunaidi. Traffic Vibrations in Buildings, 2000.

[68] H. J. Mamin, H. Birk, P. Wimmer, and D. Rugar. High-speed scanning tunneling microscopy: Principles and applications. *Applied Physics*, 75:161, 1994.

[69] J. Kim, J. Huang, and A. de Lozanne. Honeycomb lattice of graphite probed by scanning tunneling microscopy with a carbon nanotube tip. *arXiv*, 2013.

[70] Y. Wang, Y. Ye, and K. Wu. Simultaneous observation of the triangular and honeycomb structures on highly oriented pyrolytic graphite at room temperature: An STM study. *Surface Science*, 600:729–734, 2006.

[71] M. Ishigami, J. H. Chen, W. G. Cullen, M. S. Fuhrer, and E. D. Williams. Atomic Structure of Graphene on SiO_2. *Nano Lett.*, 7, 2007.

[72] E. Stolyarova, K. T. Rim, S. Ryu, J. Maultzsch, P. Kim, L. E. Brus, T.F. Heinz, M. S. Hybertsen, and G. W. Flynn. High-resolution scanning tunneling microscopy imaging of mesoscopic graphene sheets on an insulating surface. *PNAS*, 104, 2007.

[73] E. Cisternas, F. Stavale, M. Flores, C. A. Achete, and P. Vargas. First-principles calculation and scanning tunneling microscopy study of highly oriented pyrolytic graphite (0001). *Phys. Rev. B*, 79:205431, 2009.

[74] H. S. Wong, C. Durkan, and Chandrasekhar N. Tailoring the local interaction between graphene layers in graphite at the atomic scale and above using scanning tunneling microscopy. *ACS Nano*, 3:3455, 2009.

[75] M. H. Whangbo and E. Canadell. Analogies between the Concepts of Molecular Chemistry and Solid-State Physics concerning Structural Instabilities. Electronic Origin of the Structural Modulations in Layered Transition-Metal Dichalcogenides. *J. Am. Chem. Soc.*, 114:9587–9600, 1992.

[76] C. M. Fang et al. Electronic structures of ReS_2, $ReSe_2$ and TcS_2 in the real and the hypothetical undistorted structures. *Condensed Matter*, 9:4411, 1997.

[77] Daniel A. Chenet, O. Burak Aslan, Pinshane Y. Huang, Chris Fan, Arend M. van der Zande, Tony F. Heinz, and James C. Hone. In-Plane Anisotropy in Mono- and Few-Layer ReS2 Probed by Raman Spectroscopy and Scanning Transmission Electron Microscopy. *Nano Letters*, 15(9):5667–5672, 2015. PMID: 26280493.

[78] I. Gutierrez-Lezama et al. Electroluminescence from indirect band gap semiconductor ReS_2. *2D Materials*, 3, 2016.

[79] M. Gehlmann et al. Direct Observation of the Band Gap Transition in Atomically Thin ReS_2. *Nano Letters*, 17, 2017.

[80] J. L. Webb et al. Electronic band structure of ReS_2 by high-resolution angle-resolved photoemission spectroscopy. *Physical Review B*, 96, 2017.

[81] K. Keyshar et al. Chemical Vapor Deposition of Monolayer Rhenium Disulfide (ReS_2). *Advanced Materials*, 27, 2015.

[82] E. Zhang et al. ReS_2-Based Field-Effect Transistors and Photodetectors. *Advanced Functional Materials*, 25, 2015.

[83] B. Jariwala et al. Synthesis and Characterization of ReS_2 and $ReSe_2$ Layered Chalcogenide Single Crystals. *Chemistry of Materials*, 28:3352–3359, 2016.

[84] S. Yu et al. Strain-engineering the anisotropic electrical conductance in ReS_2 monolayer. *Applied Physics Letters*, 108, 2016.

[85] Sefaattin Tongay, Hasan Sahin, Changhyun Ko, Alex Luce, Wen Fan, Kai Liu, Jian Zhou, Ying-Sheng Huang, Ching-Hwa Ho, Jinyuan Yan, D. Frank Ogletree, Shaul Aloni, Jie Ji, Shushen Li adn Jingbo Li, F. M. Peeters, and Junqiao Wu. Monolayer behaviour in bulk ReS_2 due to electronic and vibrational decoupling. *Nature*, 5(3252), 2014.

[86] K. Dileep et al. Layer specific optical band gap measurement at nanoscale in MoS_2 and ReS_2 van der Waals compounds by high resolution electron energy loss spectroscopy. *Journal of Applied Physics*, 119, 2016.

[87] C. H. Ho and C. E. Huang. Optical property of the near band-edge transitions in rhenium disulfide and diselenide. *Journal of Alloys and Compounds*, 383, 2004.

[88] E. Liu et al. Integrated Digital Inverters Based on Two-dimensional Anisotropic ReS_2 Field-effect Transistors. *Nature Comm.*, 6:6991, 2015.

[89] Y. Lin et al. Single-layer res2: Two-dimensional semiconductor with tunable in-plane anisotropy. *ACS Nano*, 9, 2015.

[90] A. McCreary et al. Intricate Resonant Raman Response in Anisotropic ReS_2. *Nano Letters*, 17, 2017.

[91] A. Dathbun, Y. Kim, S. Kim, Y. Yoo, M.-S. Kang, C. Lee, and J.-H. Cho. Large-area cvd-grown sub-2 v res_2 transistors and logic gates. *Nano Letters*, 17(5):2999–3005, 2017.

[92] A. Cho, S. Namgung, H. Kim, and J. Kwon. Electric and photovoltaic characteristics of a multi-layer res_2/$rese_2$ heterostructure. *APL Materials*, 5:076101, 2017.

[93] Lewis Hart, Sara Dale, Sarah Hoye, James L. Webb, and Daniel Wolverson. Rhenium dichalcogenides: Layered semiconductors with two vertical orientations. *Nano Letters*, 16(2):1381–1386, 2016. PMID: 26799768.

[94] Ignacio Gutiérrez-Lezama, Bojja Aditya Reddy, Nicolas Ubrig, and Alberto F Morpurgo. Electroluminescence from indirect band gap semiconductor ReS_2. *2D Materials*, 3(4):045016, 2016.

[95] K. K. Tiong et al. The electrical transport properties of ReS_2 and $ReSe_2$ layered crystals. *Solid State Comm.*, 111, 1999.

[96] T. Fujita. Chemically exfoliated ReS_2. *Nanoscale*, 6:12458, 2014.

[97] H. H. Murray, S. P. Kelty, and R. R. Chianelli. Structure of Rhenium Disulfide. *ACS*, 33:19, 1994.

[98] B. A. Parkinson, J. Ren, and M. H. Whangbo. Relationship of STM and AFM Images to the Local Density of States in the Valence and Conduction Bands of $ReSe_2$. *ACS*, 113:21, 1991.

[99] S. P. Kelty, A. F. Ruppert, R. R. Chianelli, J. Ren, and M. H. Whangbo. Scanning Probe Microscopy Study of Layered Dichalcogenide ReS_2. *ACS*, 116:7857–7863, 1994.

[100] K. Friemelt, S. Akari, M. Ch. Lux-Steiner, Schill T., E. Bucher, and K. Dransfeld. Scanning tunneling microscopy with atomic resolution on ReS_2 single crystals grown by vapor phase transport. *Annalen der Physik*, 1:248–253, 1992.

[101] K. O. Obodo et al. Influence of transition metal doping on the electronic and optical properties of ReS_2 and ReS $_2$ monolayers. *Physical Chemistry - Chemical Physics*, 19, 2017.

[102] J. Kang et al. Layer-by-Layer Sorting of Rhenium Disulfide via High-Density Isopycnic Density Gradient Ultracentrifugation. *Nano Letters*, 16, 2016.

[103] O. B. Aslan et al. Linearly Polarized Excitons in Single- and Few-Layer ReS_2 Crystals. *ACS Photonics*, 3, 2015.

[104] S. Jung, T. Jeong, J. Shim, S. Park, J. Park, B. Shin, and Young Jae Song. Atomic-registry-dependent electronic structures of sulfur vacancies in res 2 studied by scanning tunneling microscopy/spectroscopy. 07 2018.

[105] D. Cakir. Doping of rhenium disulfide monolayers: a systematic first principles study. *Phys. Chem. Chem. Phys.*, 16:16771, 2014.

[106] P. Gray. Tunneling from metal to semiconductors. 1965.

[107] P. Gray. Investigating individual arsenic dopant atoms in silicon using low-temperature scanning tunnelling microscopy. 2013.

[108] Giang D. Nguyen, Liangbo Liang, Qiang Zou, Mingming Fu, Akinola D. Oyedele, Bobby G. Sumpter, Zheng Liu, Zheng Gai, Kai Xiao, and An-Ping Li. 3d imaging and manipulation of subsurface selenium vacancies in $pdse_2$. *Phys. Rev. Lett.*, 121:086101, Aug 2018.

[109] D. H. Lee and J. A. Gupta. Tunable control over the ionization state of single mn acceptors in gaas with defect-induced band bending. 2008.

[110] Z. Qiu et al. Resolving the spatial structures of bound hole states in black phosphorus. 2017.

[111] B. Kiraly et al. Probing single vacancies in black phosphorus at the atomic level. 2017.

[112] Yu, E. T. and McCaldin, J. O. and McGill, T. C. Band offsets in semiconductor heterojunctions. 1992.

[113] R. M. Feenstra, Y. Dong, M. P. Semtsiv, and W. T. Masselink. Influence of tip-induced band bending on tunnelling spectra of semiconductor surfaces. *Nanotechnology*, 18(4):044015, 2007.

[114] M. McEllistrem, G. Haase, D. Chen, and R. J. Hamers. Electrostatic sample-tip interactions in the scanning tunneling microscope. *Phys. Rev. Lett.*, 70:2471–2474, Apr 1993.

[115] J. Bardeen. Surface states and rectification at a metal semi-conductor contact. *Phys. Rev.*, 71:717–727, May 1947.

[116] D. Wong et al. Characterization and manipulation of individual defects in insulating hexagonal boron nitride using scanning tunneling microscopy. 2015.

[117] A. Depuydt, C. Van Haesendonck, N. S. Maslova, V. I. Panov, S. V. Savinov, and P. I. Arseev. Scanning tunneling microscopy and spectroscopy at low temperatures of the (110) surface of te-doped gaas single crystals. *Phys. Rev. B*, 60:2619–2626, Jul 1999.

[118] R. Dombrowski, Chr. Steinebach, Chr. Wittneven, M. Morgenstern, and R. Wiesendanger. Tip-induced band bending by scanning tunneling spectroscopy of the states of the tip-induced quantum dot on inas(110). *Phys. Rev. B*, 59:8043–8048, Mar 1999.

[119] M. C. M. M. van der Wielen, A. J. A. van Roij, and H. van Kempen. Direct observation of friedel oscillations around incorporated si_{ga} dopants in gaas by low-temperature scanning tunneling microscopy. *Phys. Rev. Lett.*, 76:1075–1078, Feb 1996.

[120] M. Wenderoth, M. A. Rosentreter, K. J. Engel, A. J. Heinrich, M. A. Schneider, and R. G. Ulbrich. Low-temperature scanning tunneling spectroscopy as a probe for a confined electron gas. *EPL (Europhysics Letters)*, 45(5):579, 1999.

[121] S. Loth. *Atomic scale images of acceptors in III-V semiconductors.* 2008.

[122] S. Horzum et al. Formation and stability of point defects in monolayer rhenium disulfide. *Phys. Rev. B.*, 89:155433, 2014.

[123] K. Teichmann et al. Controlled charge switching on a single donor with a scanning tunneling microscope. 2008.

[124] Tutiš, E. and Forró, L. and Berger, H. and Akrap, A. and Kusmartseva, A. F. and Sipos, B. From Mott state to superconductivity in 1T-TaS_2. *Nature Publishing Group*, 7(10):960, 2008.

[125] Y. Liu et al. New superconductivity in layered 1t-tas2-xsex single crystals fabricated by chemical vapor transport. *arXiv*, page 1303.6715, 03 2013.

[126] Nagata et al., S. Superconductivity in the layered compound 2h-tas2. *Journal of Physics and Chemistry of Solids*, 53(10):1259–1263, 1992.

[127] Y. Yu et al. Gate-tunable phase transitions in thin flakes of 1T-TaS_2. *Nature Nanotechnology*, 10(3):270–276, 2015.

[128] V. Iancu, A. Deshpande, and S.-W. Hla. Manipulating Kondo Temperature via Single Molecule Switching. *Nano Letters*, 6, 2006.

[129] C. P. Lu, M. Rodriguez-Vega, G. Li, A. Luican-Mayer, K. Watanabe, T. Taniguchi, E. Rossi, and E. Y. Andrei. Local, global, and nonlinear screening in twisted double-layer graphene. *Proceedings of the National Academy of Sciences*, 113(24):6623–6628, 2016.

[130] A. Pálinkás, G. Molnár, C. Hwang, L. P. Biró, and Z. Osváth. Determination of the stm tip-graphene repulsive forces by comparative stm and afm measurements on suspended graphene. *RSC Adv.*, 6:86253–86258, 2016.

[131] R. Zan, U. Bangert, C. Muryn, P. Mattocks, Hamilton B., and K. S. Novoselov. Scanning tunnelling microscopy of suspended graphene. *Journal of Physics: Conference Series*, 371(1):012070, 2012.

[132] Kendal W Clark. *STM Study of Molecular and Biomolecular Electronic Systems*. PhD thesis, Russ College of Engineering and Technology of Ohio University, 2010.